catalysts

MDPI

Article

Preparation and Property Characterization of $Eu_2SmSbO_7/ZnBiEuO_4$ Heterojunction Photocatalysts and Photocatalytic Degradation of Chlorpyrifos under Visible Light Irradiation

Jingfei Luan [1,2,*], Yichun Wang [1], Ye Yao [1], Liang Hao [1], Jun Li [1] and Yu Cao [1]

[1] School of Physics, Changchun Normal University, Changchun 130032, China; yichun2000@126.com (Y.W.); yaoye1109@mails.jlu.edu.cn (Y.Y.); hliang0725@163.com (L.H.); lijun929@126.com (J.L.); cyccsfnu0916@yeah.net (Y.C.)

[2] State Key Laboratory of Pollution Control and Resource Reuse, School of the Environment, Nanjing University, Nanjing 210093, China

* Correspondence: jfluan@nju.edu.cn; Tel.: +86-(0)-199-519-394-98

Abstract: Eu_2SmSbO_7 and $ZnBiEuO_4$ were synthesized for the first time using the hydrothermal method. $Eu_2SmSbO_7/ZnBiEuO_4$ heterojunction photocatalyst (EZHP) was synthesized for the first time using the solvothermal method. The crystal cell parameter of Eu_2SmSbO_7 was 10.5547 Å. The band gap width of Eu_2SmSbO_7 was measured and found to be 2.881 eV. The band gap width of $ZnBiEuO_4$ was measured and found to be 2.571 eV. EZHP efficiently degraded the pesticide chlorpyrifos under visible light irradiation (VLID). After VLID of 160 min, the conversion rate of the chlorpyrifos concentration reached 100%, while the conversion rate of the total organic carbon (TOC) concentration was 98.02% using EZHP. After VLID of 160 min, the photocatalytic degradation conversion rates of chlorpyrifos using EZHP were 1.13 times, 1.19 times, and 2.84 times those using Eu_2SmSbO_7, $ZnBiEuO_4$, and nitrogen-doped titanium dioxide (N-doped TiO_2), respectively. The photocatalytic activity could be ranked as follows: EZHP > Eu_2SmSbO_7 > $ZnBiEuO_4$ > N-doped TiO_2. The conversion rates of chlorpyrifos were 98.16%, 97.03%, 96.03%, and 95.06% for four cycles of experiments after VLID of 160 min using EZHP. This indicated that EZHP was stable and could be reused. In addition, the experiments with the addition of capture agents demonstrated that the oxidation removal ability of three oxidation free radicals for degrading chlorpyrifos obeyed the following order: hydroxyl radical > superoxide anion > holes. This study examined the intermediates of chlorpyrifos during the photocatalytic degradation of chlorpyrifos, and a degradation path was proposed, at the same time, the degradation mechanism of chlorpyrifos was revealed. This study provides a scientific basis for the development of efficient heterojunction photocatalysts.

Keywords: Eu_2SmSbO_7; $Eu_2SmSbO_7/ZnBiEuO_4$ heterojunction photocatalyst; chlorpyrifos; visible light irradiation; photocatalytic activity; photocatalytic degradation; degradation mechanism

Citation: Luan, J.; Wang, Y.; Yao, Y.; Hao, L.; Li, J.; Cao, Y. Preparation and Property Characterization of $Eu_2SmSbO_7/ZnBiEuO_4$ Heterojunction Photocatalysts and Photocatalytic Degradation of Chlorpyrifos under Visible Light Irradiation. *Catalysts* **2024**, *14*, 144. https://doi.org/10.3390/catal14020144

Academic Editors: Jose L. Hueso, Ewa Kowalska and Zhishun Wei

Received: 26 November 2023
Revised: 24 January 2024
Accepted: 7 February 2024
Published: 15 February 2024

1. Introduction

In recent years, there has been an increasing demand for food supplies due to the growing global population [1–3]. The use of pesticides is a valid method to increase crop yields [4–7]. Therefore, pesticides are widely used in agricultural production. However, usually only a small amount of the pesticide works, and most of the pesticide remains on the crop or in the soil. Pesticide residues on crops can be harmful to creatures, and other residues can cause serious pollution of the soil and even the underground water [8–11]. Chlorpyrifos, as one of the classical organophosphorus pesticides, has been widely used due to its low cost and effective ability to control pests, weeds, and diseases [12–15]. However, the disadvantages of chlorpyrifos are also obvious; for example, chlorpyrifos is

an organic pollutant that is difficult to degrade; at the same time, chlorpyrifos also affects the neurological system, leading to various diseases [16–20]. Moreover, chlorpyrifos has adverse effects on the development of the brain and body, especially for children [21,22]. Therefore, elimination of chlorpyrifos derived from wastewater is a meaningful goal, considering the healthy living environment for humans.

After preliminary physical filtration, some methods have been invented for the degradation of small particle organic pollutants that are easily dissolved in water, such as chlorination, electrocatalysis, and anaerobic–aerobic biological treatment [23–31]. All the above methods have some drawbacks. For example, chlorination is hard to degrade completely. Moreover, electrocatalytic methods consume more energy, and, ultimately, the anaerobic–aerobic biological treatment requires complicated reaction conditions. Therefore, finding a method with higher degradation efficiency to solve the problem of organic pollutants is needed.

A promising method, photocatalytic technology, was reported to be an effective way of degrading organic pollutants [32–39]. Photocatalytic technology absorbs solar energy to degrade water, generating free radicals with significant oxidizing and reducing properties. The free radicals can degrade organic pollutants without producing secondary pollution. Photocatalytic technology has become a favored choice due to its advantages of high efficiency, non-toxicity, low cost, and environmental friendliness [40–42].

At the beginning, TiO_2 became a popular research area in the field of photocatalysis due to its simple fabrication process, high photocatalytic activity, and excellent stability [43–45]. With TiO_2 as a catalytic material, it was required that the incident photon energy must be higher than 3.2 eV, and only ultraviolet light would be able to satisfy this condition. At the same time, ZnO was also reported as the photocatalyst using ultraviolet light [46,47]. The energy of ultraviolet light in sunlight was too small compared with visible light (which occupies 43% of the sunlight spectrum). Based on the reports of the researchers, the construction of the composite would have a wider light absorption range and higher photocatalytic efficiency than that of single metal oxides and composite catalysts [48–51]. $A_2B_2O_7$-type compounds and AB_2O_4-type compounds had been reported to have excellent catalytic performance under visible light irradiation (VLID). For example, Zou et al. found that Bi_2InNbO_7 had a good effect in decomposing water to produce hydrogen [52]. Based on our previous report, $ZnBiYO_4$ also exhibited excellent photocatalytic properties under VLID [53]. It was speculated that Eu_2SmSbO_7 and $ZnBiEuO_4$ could effectively degrade organic pollutants under VLID.

In the process of photochemical reactions, the photo-induced electrons and the photo-induced holes are generated after light irradiation on the surface of the photocatalytic material. The photo-induced electrons and the photo-induced holes participated in the subsequent reaction to generate superoxide anions and hydroxyl radicals. Superoxide radicals and hydroxyl radicals had strong redox capacity and therefore can degrade organic pollutants effectively. However, the photo-induced electrons and the photo-induced holes that do not participate in the reaction are recombined, affecting the generation of superoxide radicals and hydroxyl radicals, and thus affecting the photocatalytic efficiency. Therefore, the photocatalytic efficiency can be improved by inhibiting the recombination of the photo-induced electrons and the photo-induced holes [54,55]. The catalytic efficiency can be improved by constructing heterojunction structures to inhibit the complexation of photo-induced electrons and photo-induced holes [56,57]. For example, the heterojunction $AgBr/BiPO_4$ that was synthesized by Xu H. et al. possessed higher catalytic activity than pure $BiPO_4$, and the heterojunction $Ag_2MoO_4/Bi_4Ti_3O_{12}$ by Cheng T. T. et al. had higher catalytic activity than pure Ag_2MoO_4 or pure $Bi_4Ti_3O_{12}$ [58,59]. Thus, we synthesized the $Eu_2SmSbO_7/ZnBiEuO_4$ heterojunction photocatalyst (EZHP) and found that EZHP had excellent catalytic activity under VLID. The catalyst Ag/TiO_2 that was prepared by Fattah W. I. A. et al. achieved a conversion rate of chlorpyrifos of nearly 75% after light irradiation for 120 min [60]. The conversion rate of chlorpyrifos reached 84.5% using EZHP under VLID of 120 min in our manuscript. In conclusion, the EZHP that was prepared

by Jingfei Luan showed higher photocatalytic activity compared with the Ag/TiO_2 that was prepared by Fattah W. I. A. et al. The catalyst Cu/ZnO that was prepared by Pathania, D. et al. achieved a conversion rate of chlorpyrifos of 81% after solar light irradiation of 240 min [61]. The conversion rate of chlorpyrifos reached 100% using EZHP under VLID of 160 min in our manuscript. In summary, the EZHP that was prepared by Jingfei Luan showed higher photocatalytic activity compared with the Cu/ZnO that was prepared by Pathania, D. et al.

In this paper, the structural properties of pure-phase $ZnBiEuO_4$ and single-phase Eu_2SmSbO_7 were analyzed using an X-ray diffractometer (XRD), a UV-Vis spectrophotometer, a Fourier transform infrared (FTIR) spectrometer, a Raman spectrometer, X-ray photoelectron spectroscopy (XPS), transmission electron microscopy (TEM), energy dispersive X-ray spectroscopy (EDS), and ultraviolet photoelectron spectroscopy (UPS). In addition, the conversion rates of chlorpyrifos under VLID were measured with pure-phase Eu_2SmSbO_7, $ZnBiEuO_4$, N-doped TiO_2, or $Eu_2SmSbO_7/ZnBiEuO_4$ as a photocatalyst. The aim of this study was to prepare a novel heterojunction photocatalyst for the removal of chlorpyrifos from pesticide wastewater under VLID. Our innovative research involved the first synthesis and characterization of a novel Eu_2SmSbO_7 nanocatalyst, $ZnBiEuO_4$, and EZHP. For the first time, EZHP was used to degrade chlorpyrifos and the conversion rates of chlorpyrifos under VLID were obtained. The results showed that EZHP had high photocatalytic activity and could effectively degrade chlorpyrifos. This paper will make a huge contribution to the structural construction of novel photocatalysts and to the study of pesticide degradation.

2. Result and Discussion

2.1. XRD Analysis

X-ray diffraction (XRD) uses the diffraction of X-rays in crystals to characterize the diffracted X-ray signals and obtain information about the structure of the crystalline material, the crystal size, and cell parameters. Figure 1 shows the XRD patterns of $ZnBiEuO_4$, Eu_2SmSbO_7, and $Eu_2SmSbO_7/ZnBiEuO_4$ heterojunction photocatalyst (EZHP). As can be seen from Figure 1, the diffraction peaks of Eu_2SmSbO_7 and $ZnBiEuO_4$ could be detected in the XRD spectra of EZHP without any other diffraction peaks that belonged to the impure phase, which indicated that the EZHP was successfully synthesized.

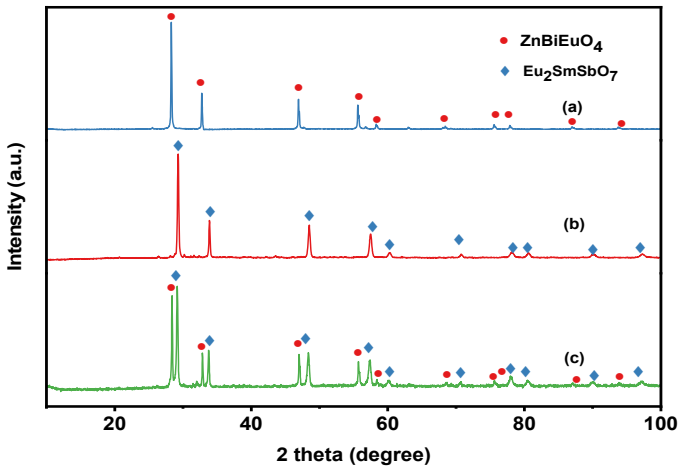

Figure 1. The XRD patterns of (**a**) $ZnBiEuO_4$, (**b**) Eu_2SmSbO_7, (**c**) EZHP (red circle: the crystal plane of $ZnBiEuO_4$; blue diamond: the crystal plane of Eu_2SmSbO_7).

Figure 2a displays the structural properties of Eu_2SmSbO_7 according to Rietveld analysis using the Materials Studio program. The results of Rietveld refinement for Eu_2SmSbO_7 showed that the observed intensities and calculated intensities of the pyrochlore-type structure were in fine agreement. Eu_2SmSbO_7 was a single-phase, cubic crystal system

with a space group of *Fd3m* (modeled to include O atoms) [62]. The atomic structure of Eu_2SmSbO_7 is shown in Figure 2b, where the cell parameter *a* for Eu_2SmSbO_7 is 10.5547 Å. Table 1 presents the atomic coordinates and the structural parameters of Eu_2SmSbO_7. The full-profile structural refinement of Eu_2SmSbO_7 generated an unweighted *R* factor, R_P = 2.14%.

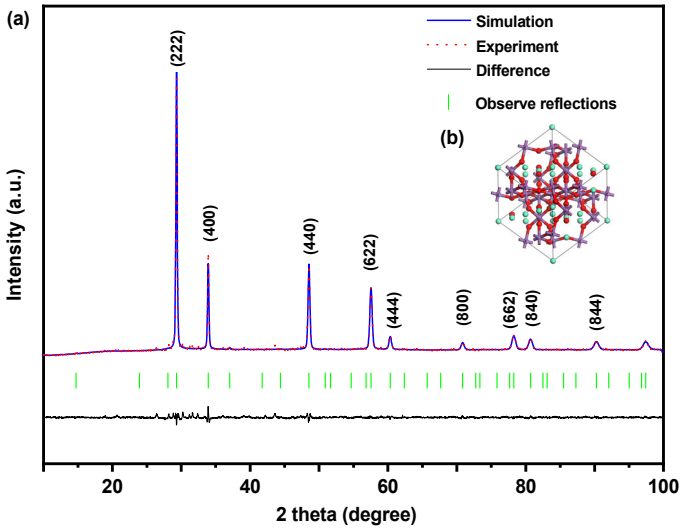

Figure 2. (**a**) XRD and Rietveld refinement of Eu_2SmSbO_7: Simulated XRD data (blue solid line), experimental XRD data (red dotted line), difference between experimental XRD data and simulated XRD data (black solid line), and observed diffraction peaks (green perpendicular lines). (**b**) Atom construction of Eu_2SmSbO_7. (Red atom: O, green atom: Eu, purple atom: Sm or Sb).

Table 1. Structural parameters of Eu_2SmSbO_7.

Atom	x	y	z	Occupation Factor
Eu	0	0	0	1
Sm	0.5	0.5	0.5	0.5
Sb	0.5	0.5	0.5	0.5
O(1)	−0.185	0.125	0.125	1
O(2)	0.125	0.125	0.125	1

The x-coordinate of the O(1) atom reflects the change in crystal structure of $A_2B_2O_7$-type compounds. If the lengths of the A-O(1) bonds (of which there are six) are identical to the lengths of the A-O(2) bonds (two), it can be assumed that x is equal to 0.375 [63]. The value of x provides information about the octahedral distortion of MO_6 (M = Sm^{3+} and Sb^{5+}). Since the x value was shifted from x = 0.375, it was proved that there existed crystal structure distortions in Eu_2SmSbO_7 [63]. The photocatalytic degradation of chlorpyrifos under VLID required charge separation to prevent photo-induced electron and photo-induced hole recombination. Deformation of MO_6 octahedra has been reported to prevent charge recombination and enhance photocatalytic performance in some photocatalysts such as $BaTi_4O_9$ and $Sr_2M_2O_7$ (M = Nb^{5+} and Ta^{5+}) [64,65]. Therefore, it was speculated that the deformation of MO_6 (M = Sm^{3+} and Sb^{5+}) octahedra in Eu_2SmSbO_7 could enhance the photocatalytic performance. Eu_2SmSbO_7 had a three-dimensional network structure which consisted of corner-sharing MO_6 (M = Sm^{3+} and Sb^{5+}) octahedra. Each Eu^{3+} ion was connected to two MO_6 octahedra to form a chain. Eu-O bonds were found in two lengths, with the six Eu-O (1) bond lengths (4.376 Å) being longer than the two Eu-O (2) bond lengths (2.285 Å). The crystal structure of Eu_2SmSbO_7 had six M-O (1) (M = Sm^{3+} and Sb^{5+}) bonds with lengths of 2.285 Å, six M-O (3) bonds with lengths of 2.285 Å, and six M-Eu (M = Sm^{3+} and Sb^{5+}) bonds with lengths of 3.732 Å. The M-O-M (M = Sm^{3+} and Sb^{5+}) bond

angle in the Eu_2SmSbO_7 crystal structure was 109.47°, the Eu-M-Eu (M = Sm^{3+} and Sb^{5+}) bond angle was 135.00°, and the Eu-M-O (M = Sm^{3+} and Sb^{5+}) bond angle was 125.26°.

Many previous studies have indicated that the size of the bond angle affects the luminescent properties of the material [63,66]. When the bond angles of M-O-M (M = Sm^{3+} and Sb^{5+}) were close to 180°, the produced photo-induced electrons and photo-induced holes were more easily accessible to the reaction sites on the catalyst surface. In addition, the larger the Eu-Sm-O bond angle or Eu-Sb-O bond angle of Eu_2SmSbO_7 was, the higher the photocatalytic activity was. The degradation of chlorpyrifos under VLID with Eu_2SmSbO_7 as a photocatalyst mainly depended on the crystal structure and electronic structure of Eu_2SmSbO_7.

Figure 3a displays the structural properties of $ZnBiEuO_4$ according to the Rietveld refinement analysis using the Materials Studio version 2.2 software. $ZnBiEuO_4$ had a tetragonal crystalline nature with the space group of *I41/A* [67]. The atomic structure of $ZnBiEuO_4$ is shown in Figure 3b. It can be found from Figure 3b that the cell parameters for $ZnBiEuO_4$ were a = b = 10.5572 Å and c = 10.0341 Å. The atomic coordinates and structural parameters of $ZnBiEuO_4$ are listed in Table 2. The full-profile structural refinement of $ZnBiEuO_4$ generated an unweighted *R* factor, R_P = 6.62%.

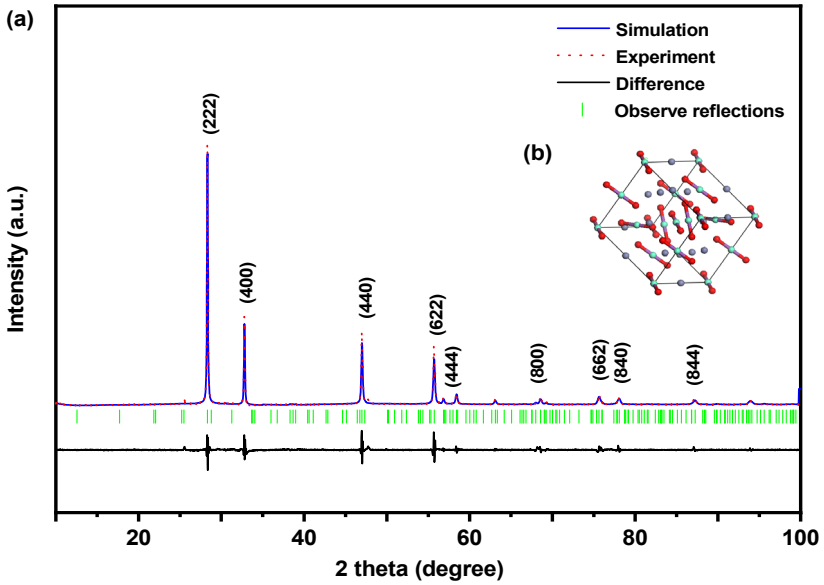

Figure 3. (**a**) XRD and Rietveld refinement of $ZnBiEuO_4$: simulated XRD data (blue solid line), experimental XRD data (red dotted line), difference between experimental and simulated XRD data (black solid line), and observed diffraction peaks (green perpendicular lines). (**b**) Atom construction of $ZnBiEuO_4$. (Red atom: O, purple atom: Zn, green atomy: Bi or Eu.).

Table 2. Structural parameters of $ZnBiEuO_4$.

Atom	x	y	z	Occupation Factor
Zn	0	0	0.5	1
Bi	0	0	0	1
Eu	0	0	0	1
O	0.75731	0.14013	0.08188	1

The crystallite size (*L*) could be calculated using the Scherrer Formula (1) [68–70]:

$$L = \frac{K\lambda}{\beta cos\theta} \quad (1)$$

K is the shape constant, normally taken as 0.9. λ is the X-ray wavelength (in this study, λ = 1.54056 Å), β is the half-width of the diffraction peak at the maximum height, and θ is the Bragg angle. Using the Scherrer formula, we could calculate the crystallite size of Eu_2SmSbO_7 (341 nm) and the crystallite size of $ZnBiEuO_4$ (522 nm). The crystallite size of Eu_2SmSbO_7 or $ZnBiEuO_4$ was 341 nm or 522 nm after the formation of the EZHP. The crystallite size of Eu_2SmSbO_7 and $ZnBiEuO_4$ did not change after the formation of the EZHP.

2.2. FTIR Analysis

The absorption peaks of functional groups and chemical bonds can be obtained from FTIR spectroscopy to determine the chemical composition of a substance. Figure 4 displays the FTIR spectra of Eu_2SmSbO_7, EZHP, and $ZnBiEuO_4$, including the characteristic absorption peaks associated with the Eu–O, Sm–O, Sb–O–Sb, Zn–O, and Bi–O bonds. The stretching vibrations of Eu–O or Sm–O bonds appeared at 590 cm^{-1}or 508 cm^{-1}, respectively [71,72]. The peaks at 728 cm^{-1} and 649 cm^{-1} were related to the bending vibrations of the Sb–O–Sb bond [73,74]. The bending vibration of Zn–O bond appeared at 468 cm^{-1} and the bending vibration of Bi–O bond was associated with the characteristic peak at 429 cm^{-1} [75,76]. The peak at 1631 cm^{-1} was related to the bending vibration of the O–H group [77]. The multiple bands that were observed from 1361 cm^{-1} to 1631 cm^{-1} corresponded to the vibrations of the C–H bonds [78].

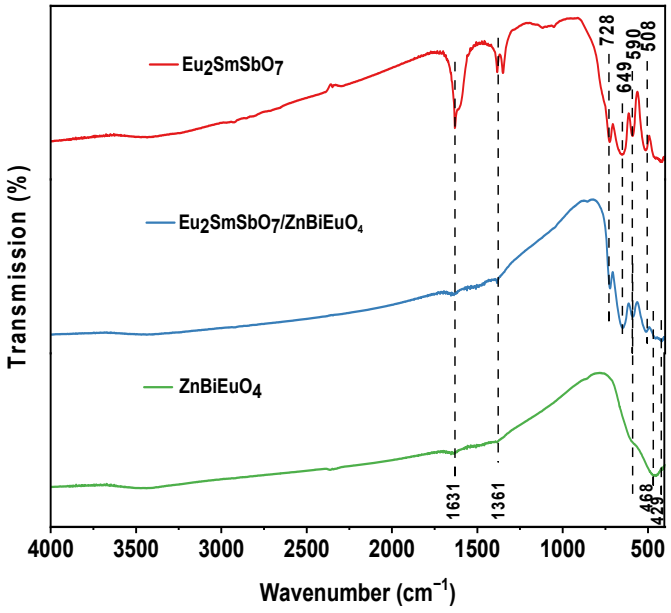

Figure 4. FTIR spectra of Eu_2SmSbO_7, EZHP, and $ZnBiEuO_4$.

2.3. Raman Analysis

Raman spectroscopy is based on the interaction of chemical bonds within a substance and can reflect the chemical structure of the substance. The Raman spectra of $ZnBiEuO_4$, Eu_2SmSbO_7, and EZHP are presented in Figure 5. The characteristic peaks of Zn–O, Eu–O, or Bi–O which were found in the Raman spectrum of $ZnBiEuO_4$ appeared at 278 cm^{-1}, 438 cm^{-1}, or 631 cm^{-1}, respectively [79–81]. In the Raman spectrum of Eu_2SmSbO_7, the characteristic peaks of Eu–O appeared at 366 cm^{-1}, 450 cm^{-1}, and 707 cm^{-1}; at the same time, the characteristic peaks of Sm–O appeared at 168 cm^{-1} [80,82]. The peaks at 224 cm^{-1}, 281 cm^{-1}, 472 cm^{-1}, and 527 cm^{-1}, which are displayed in Figure 5, belonged to Sb–O and Sb–O–Sb [83,84]. Furthermore, the Raman spectrum of the EZHP included different absorption peaks which were derived from Eu_2SmSbO_7 and $ZnBiEuO_4$, including peaks at 163 cm^{-1}, 225 cm^{-1}, 275 cm^{-1}, 288 cm^{-1}, 367 cm^{-1}, 440 cm^{-1}, 454 cm^{-1}, 471 cm^{-1},

536 cm^{-1}, 625 cm^{-1}, and 706 cm^{-1}. The above results provide indirect evidence for our successful preparation of $ZnBiEuO_4$, Eu_2SmSbO_7, and EZHP.

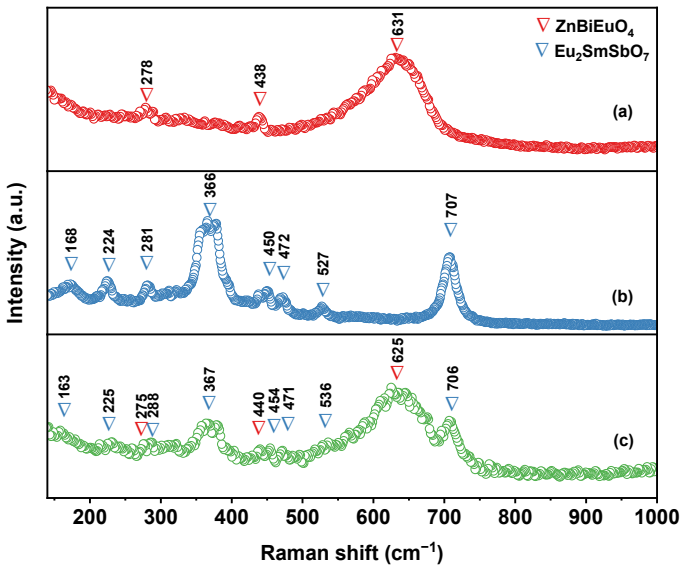

Figure 5. Raman spectra of (**a**) $ZnBiEuO_4$, (**b**) Eu_2SmSbO_7, and (**c**) EZHP.

2.4. XPS Analysis

X-ray photoelectron spectroscopy can provide information on elemental composition, atomic valence, and elemental content. XPS analysis was carried out in order to study the chemical compositions and valence states of each element in Eu_2SmSbO_7, EZHP, and $ZnBiEuO_4$. Figure 6 illustrates the XPS spectra of Eu_2SmSbO_7, EZHP, and $ZnBiEuO_4$. From Figure 6 it can be seen that the prepared sample of Eu_2SmSbO_7, $ZnBiEuO_4$, or EZHP was successfully synthesized. In addition, a carbon peak was observed and this carbon peak was attributed to adventitious hydrocarbon as a calibration reference.

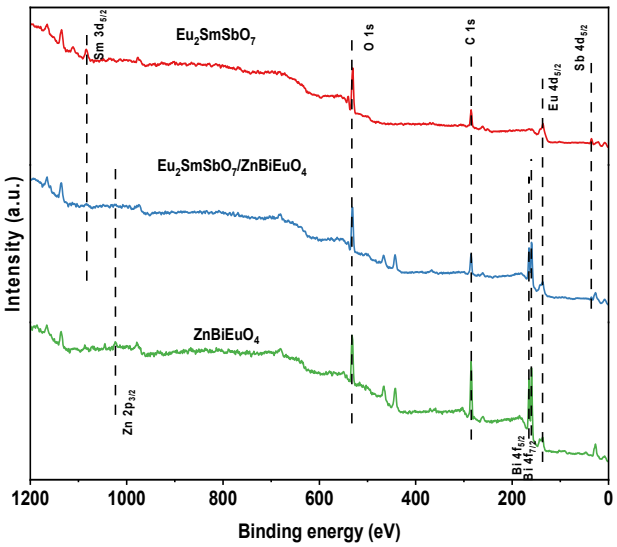

Figure 6. XPS spectra of Eu_2SmSbO_7, EZHP, and $ZnBiEuO_4$.

Figure 7a–e shows the spectral peaks of Sm 3d, Sb 4d, Eu 4d, Zn 2p, and Bi 4f in Eu_2SmSbO_7, $ZnBiEuO_4$, and EZHP. These peaks were located at 1084.25 eV (Sm $3d_{5/2}$), 34.53 eV (Sb $4d_{5/2}$), 135.91 eV (Eu $4d_{5/2}$), 135.83 eV (Eu $4d_{5/2}$), 1022.30 eV (Zn $2p_{3/2}$), 159.33 eV (Bi $4f_{7/2}$), and 164.70 eV (Bi $4f_{5/2}$), respectively. In EZHP, these peaks were slightly

shifted towards higher binding energies, such as 1084.48 eV (Sm $3d_{5/2}$), 34.76 eV (Sb $4d_{5/2}$), 136.06 eV (Eu $4d_{5/2}$), 1022.45 eV (Zn $2p_{3/2}$), 159.48 eV (Bi $4f_{7/2}$), and 164.85 eV (Bi $4f_{5/2}$). This confirmed the existence of a strong interfacial interaction between Eu_2SmSbO_7 and $ZnBiEuO_4$. The reason for this phenomenon could be the electron transfer and delocalization between Eu_2SmSbO_7 and $ZnBiEuO_4$ in the heterojunction photocatalyst. Furthermore, in $ZnBiEuO_4$ and EZHP, the spin-orbit separation value between Bi $4f_{7/2}$ and Bi $4f_{5/2}$ was determined to be 5.37 eV, which indicated that Bi^{3+} was exclusively present. Figure 7f presents the deconvolution O 1s spectrum of EZHP. The peak at 531.28 eV was assigned to O 1s. In addition, the peaks at 531.83 eV and 540.14 eV corresponded to Sb $3d_{5/2}$ and Sb $3d_{3/2}$, respectively.

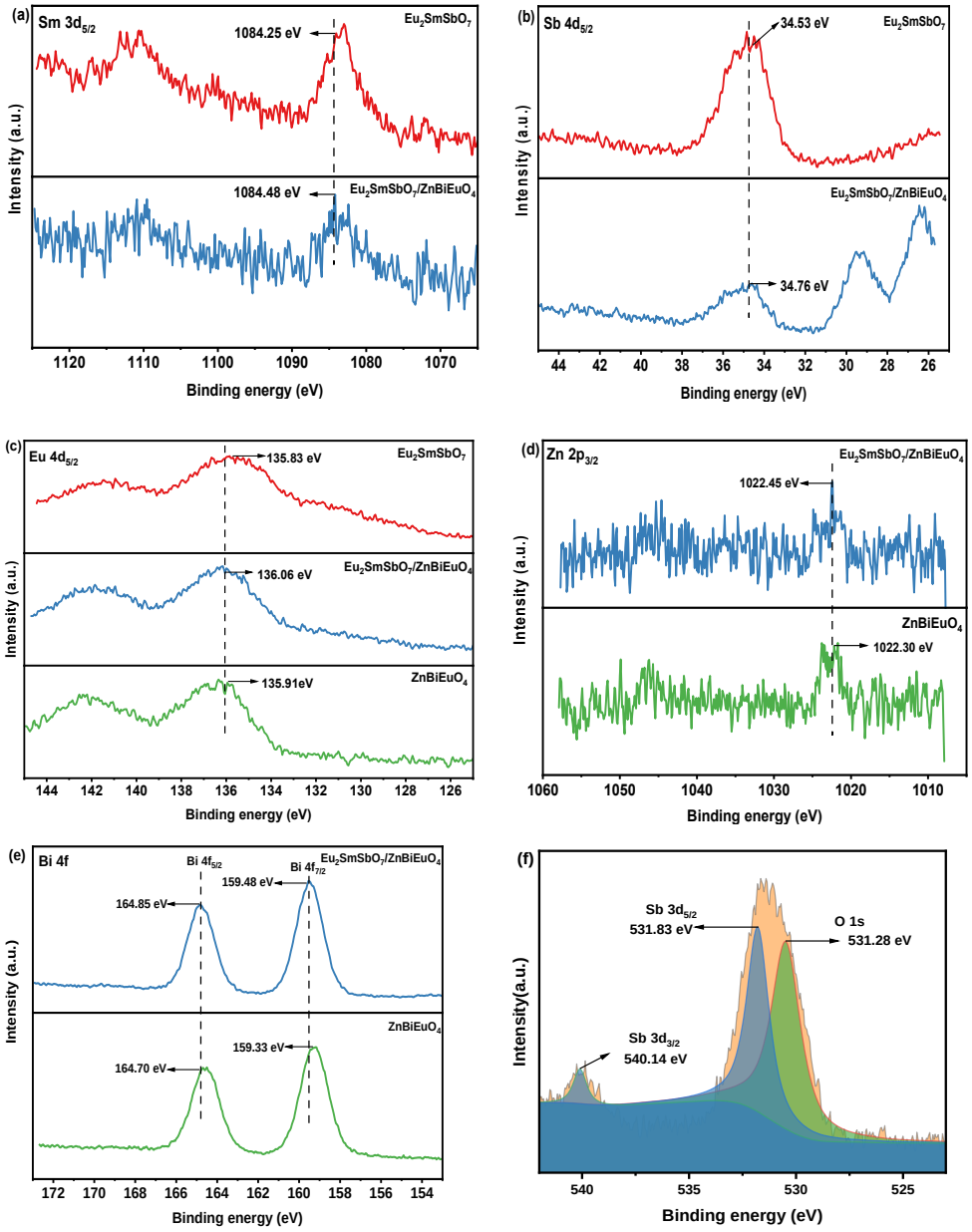

Figure 7. XPS spectrum of (**a**) Sm^{3+}, (**b**) Sb^{5+}, (**c**) Eu^{3+}, (**d**) Zn^{2+}, and (**e**) Bi^{3+} for EZHP, Eu_2SmSbO_7, and $ZnBiEuO_4$, and (**f**) XPS spectrum of O^{2-} in EZHP.

The results of XPS analysis showed that the oxidation states of Eu, Sm, Sb, Zn, Bi, and O ions within Eu_2SmSbO_7, $ZnBiEuO_4$, and EZHP were +3 [85], +3 [86], +5 [87–89], +2 [90], +3 [91,92], and −2 [93]. According to the results of XPS analysis, the surface elemental

analyses result for EZHP indicated that the average atomic ratio of Eu:Sm:Sb:Zn:Bi:O was 934:314:301:323:337:7791. According to the results of XPS analysis, the surface atomic concentration ratio of Eu:Sm:Sb:Zn:Bi:O was 9.34%:3.14%:3.01%:3.23%:3.37%:77.91% for EZHP. In the EZHP sample, the atomic ratios of Eu:Sm:Sb and Zn:Bi:Eu were 2.06:1.04:1.00 and 1.03:1.08:1.00, respectively. Obviously, neither shoulders nor widening of the XPS peaks for Eu_2SmSbO_7 or $ZnBiEuO_4$ were observed, which indicated the absence of any other phases.

2.5. UV-Vis Diffuse Reflectance Spectra

UV–visible diffuse reflectance is a commonly used spectral analysis technique that can be used to determine the bandgap width of a material. Figure 8a illustrates the absorption spectrum of Eu_2SmSbO_7. Figure 8b shows the plot of $(\alpha h\nu)^2$ and $h\nu$ for Eu_2SmSbO_7. Figure 9a illustrates the absorption spectrum of $ZnBiEuO_4$. Figure 9b shows the plot of $(\alpha h\nu)^{1/2}$ and $h\nu$ for $ZnBiEuO_4$. Figure 10a illustrates the absorption spectrum of EZHP. Figure 10b shows the plot of $(\alpha h\nu)^{1/2}$ and $h\nu$ for EZHP. The absorption edge of the novel photocatalyst Eu_2SmSbO_7 was at 430 nm; at the same time, the absorption edge of EZHP was at 453 nm and the absorption edge of $ZnBiEuO_4$ was at 482 nm. The three above catalysts had absorption edges in the visible range. Through the point of intersection of the $h\nu$ (photon energy)-axis with the prolonging of the linear part of the absorption edge of the Kubelka–Monk function (2) (re-emission function), the bandgap energy of the semiconductor could be determined [94,95].

$$\frac{[1 - R_d(h\nu)]^2}{2R_d(h\nu)} = \frac{\alpha(h\nu)}{S} \quad (2)$$

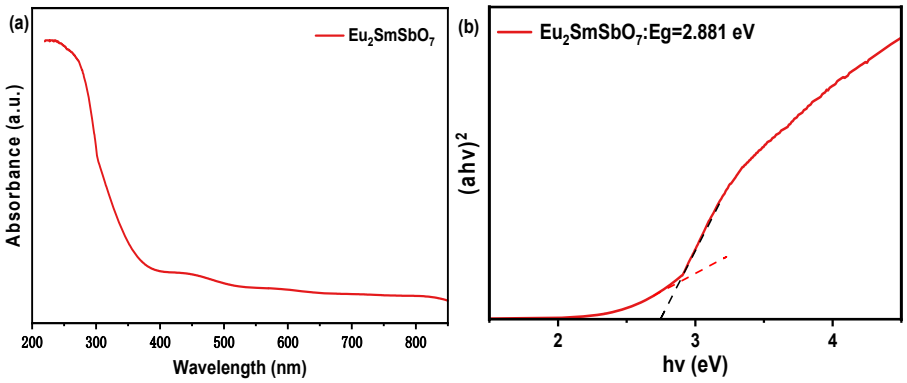

Figure 8. (**a**) The UV-Vis diffuse reflectance spectrum of Eu_2SmSbO_7; (**b**) plots of $(\alpha h\nu)^2$ and $h\nu$ for Eu_2SmSbO_7 (black dashed line: the linear fit of the correlative diagram; red dashed line: base line).

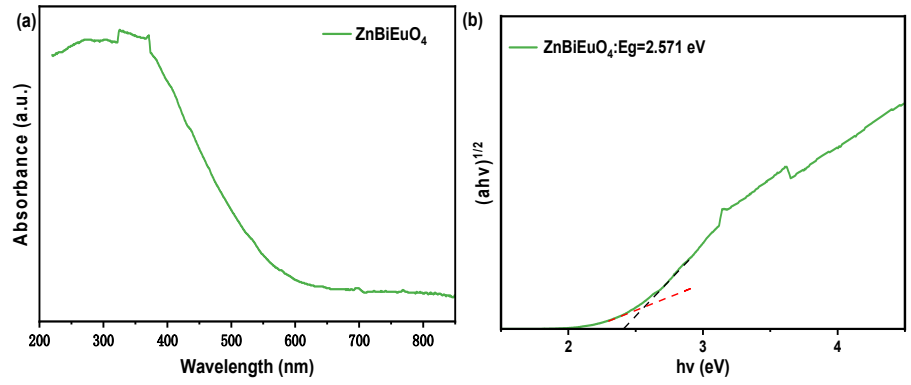

Figure 9. (**a**) The UV-Vis diffuse reflectance spectrum of $ZnBiEuO_4$; (**b**) plots of $(\alpha h\nu)^{1/2}$ and $h\nu$ for $ZnBiEuO_4$ (black dashed line: the linear fit of the correlative diagram; red dashed line: base line).

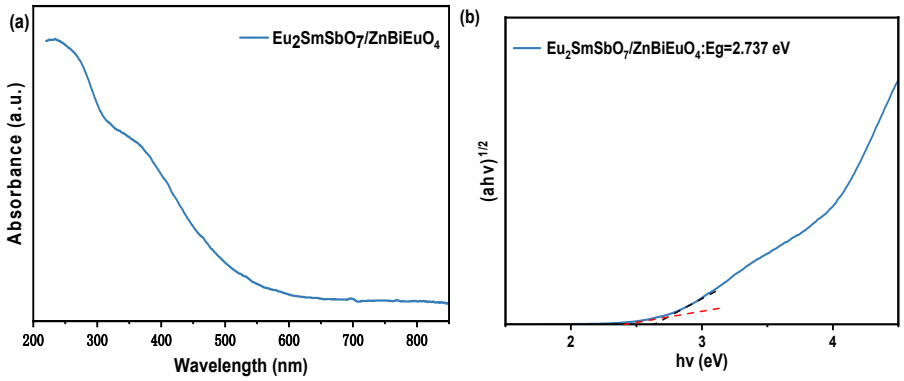

Figure 10. (**a**) The UV-Vis diffuse reflectance spectrum of EZHP; (**b**) plots of $(\alpha h\nu)^{1/2}$ and $h\nu$ for EZHP (black dashed line: the linear fit of the correlative diagram; red dashed line: base line).

In above equations, S, R_d, and α represents the scattering quotiety, diffuse reflectance, and radiation absorption quotiety, respectively.

Photo-absorption near the band edge of the crystalloid semiconductor follows Equation (3) [96,97]:

$$\alpha h\nu = A\left(h\nu - E_g\right)^n \quad (3)$$

In this equation, A, α, E_g, and ν represent the proportional constant, absorption coefficient, band gap, and light frequency, respectively. The value of n controls the transition property of the semiconductor. The values of E_g and n could be identified by following these three steps: (1) draw a graph of $\ln(\alpha h\nu)$ with $\ln\left(h\nu - E_g\right)$ and estimate the approximate value of E_g; (2) based on the rate of slope of the graph, speculate about the value of n; (3) draw a graph of $(\alpha h\nu)^{1/n}$ with $h\nu$, refine the E_g values, and prolong the region of the curve that approximates a straight line until it intersectsthebaseline. The energy bandwidths of Eu_2SmSbO_7, EZHP, and $ZnBiEuO_4$ could be estimated using the direct method (1240/transition wavelength λ).

The black dashed line in Figures 8b, 9b, and 10b is the extrapolation line of the linear part of the absorption edge; thus, the intersection of the black dashed line with the baseline is the bandgap width [98]. According to the calculation that was conducted using above method, the E_g value of Eu_2SmSbO_7 was 2.881 eV and the E_g value of $ZnBiEuO_4$ was 2.571 eV. Similarly, it could be concluded that the E_g value of EZHP was 2.737 eV. All of the three above catalysts had a visible light response characteristic. The n value of Eu_2SmSbO_7 was estimated to be 0.5, which indicated that the optical transition was directly allowed. The n value of $ZnBiEuO_4$ or EZHP was estimated to be 2, which indicated that the optical transition was indirectly allowed.

2.6. Property Characterization of Eu_2SmSbO_7/$ZnBiEuO_4$ Heterojunction Photocatalyst

Figure 11 shows the TEM image of Eu_2SmSbO_7. Figure 12 displays the TEM image of $ZnBiEuO_4$. As can be seen from Figures 11 and 12, the particle size of Eu_2SmSbO_7 was about 350 nm, while the particle size of $ZnBiEuO_4$ was about 520 nm, which was about the same as that of the XRD analysis.

Figure 13 shows the TEM image of EZHP. Figure 14 displays EDS elemental maps of EZHP (Eu, Sm, Sb, and O for Eu_2SmSbO_7, and Zn, Bi, Eu, and O for $ZnBiEuO_4$). Figure 15 illustrates the EDS spectrum of EZHP. From Figures 11–14, it can be noticed that the larger particles belonged to $ZnBiEuO_4$ while the smaller particles belonged to Eu_2SmSbO_7. $ZnBiEuO_4$ particles were surrounded by smaller Eu_2SmSbO_7 particles, which indicated the successful synthesis of EZHP.

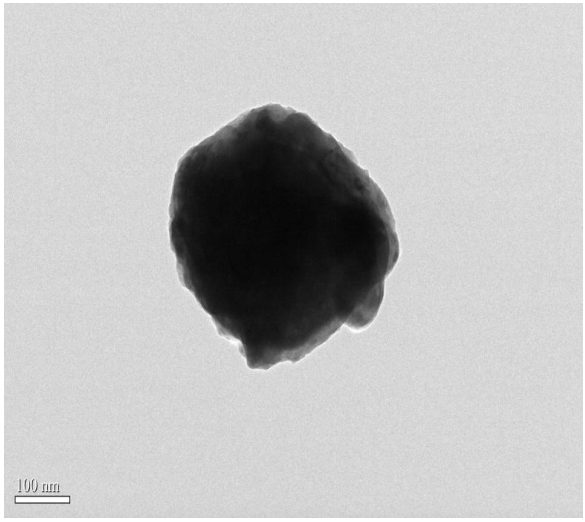

Figure 11. TEM image of Eu_2SmSbO_7.

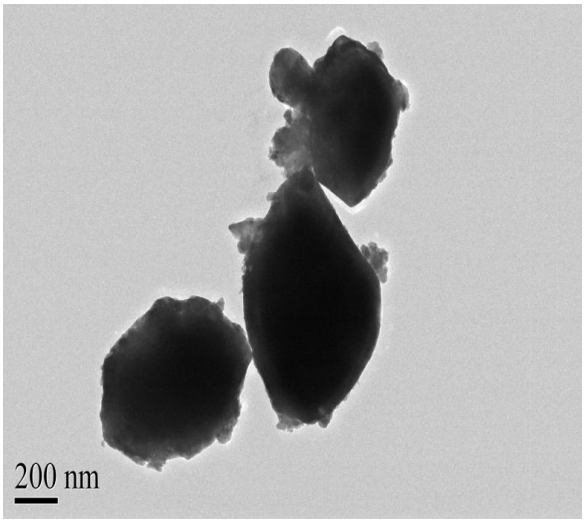

Figure 12. TEM image of $ZnBiEuO_4$.

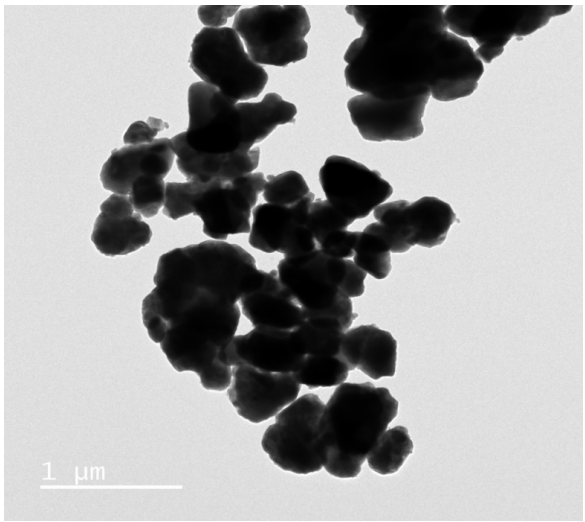

Figure 13. TEM image of EZHP.

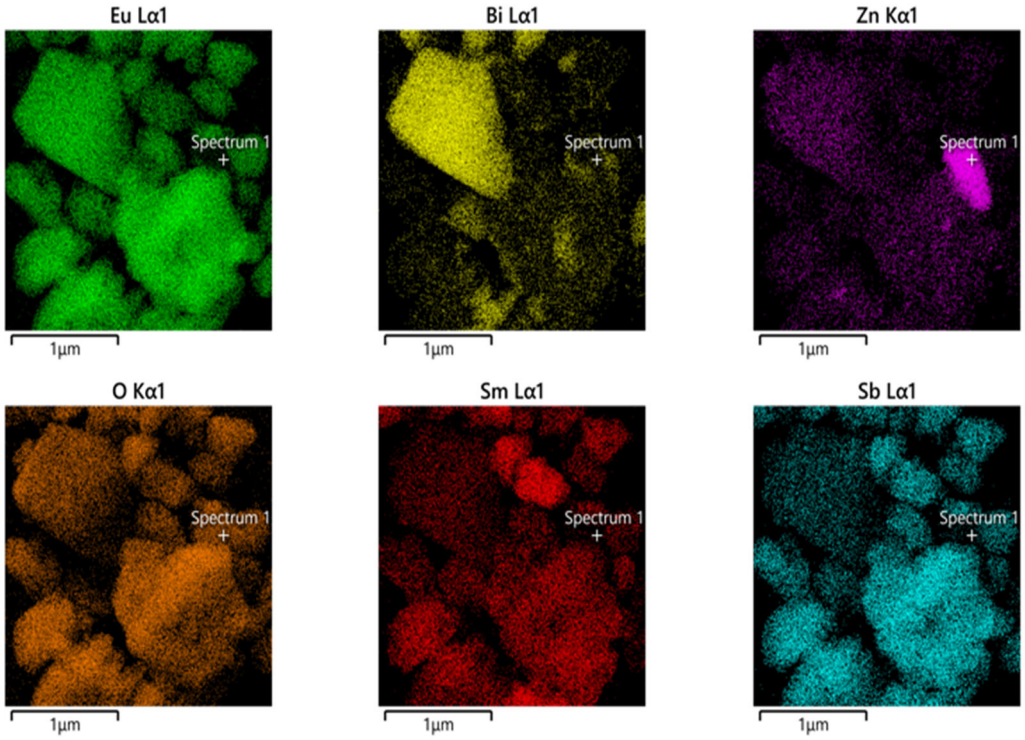

Figure 14. EDS elemental mapping of EZHP (Eu, Sm, Sb, and O from Eu_2SmSbO_7, and Zn, Bi, Sb, and O from $ZnBiEuO_4$).

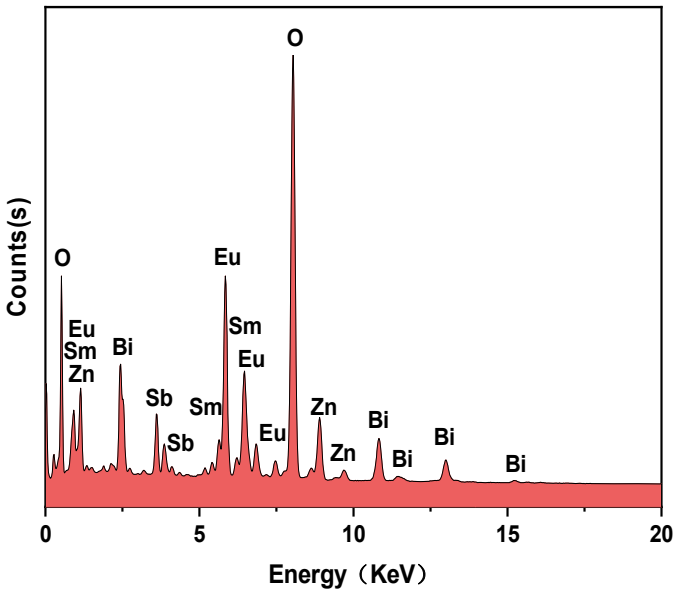

Figure 15. The EDS spectrum of EZHP.

Based on Figures 14 and 15, it could be proved that europium, samarium, antimony, zinc, bismuth, and oxygen elements were present in EZHP and there were no other impurities. It can be concluded that the EZHP that was synthesized in this study was of high purity. According to the EDS spectrum of EZHP in Figure 15, the surface atomic concentration ratio of Eu:Sm:Sb:Zn:Bi:O was 9.36%:2.94%:2.87%:3.29%:3.31%:78.23%, which was approximately the same as the results of XPS analysis.

2.7. Photocatalytic Activity

Figure 16a shows the concentration variation curves of chlorpyrifos during the photocatalytic degradation of chlorpyrifos under VLID using EZHP, Eu_2SmSbO_7, $ZnBiEuO_4$, nitrogen-doped titanium dioxide (N-doped TiO_2), or without a catalyst. N-doped TiO_2 is a widely recognized visible light responsive photocatalyst; thus, we chose to use N-doped TiO_2 for comparing the photocatalytic activity with that of other photocatalysts [99,100]. It can be obviously seen that the concentration of chlorpyrifos in pesticide wastewater gradually decreased with the extension in VLID time.

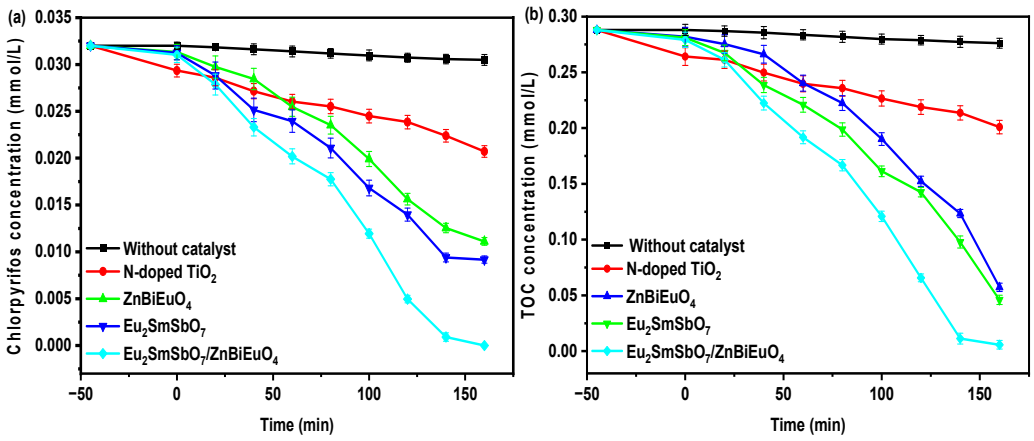

Figure 16. Concentration variation curves of (**a**) chlorpyrifos and (**b**) TOC during the photodegradation of chlorpyrifos using EZHP, Eu_2SmSbO_7, $ZnBiEuO_4$, N-doped TiO_2, or without a catalyst under VLID.The conversion rates of chlorpyrifos could be calculated by $(1 - \frac{C}{C_0}) \times 100\%$, where C represents the instantaneous concentration of chlorpyrifos and C_0 represents the initial concentration of chlorpyrifos. For a better comparison in all experiments, the VLID time was set to 160 min. By analyzing the data in Figure 16a, it can be seen that the conversion rate of chlorpyrifos during degradation of chlorpyrifos using EZHP was 100% after VLID of 160 min, with the reaction rate of 3.33×10^{-9} mol·L^{-1}·s^{-1} and a photonic efficiency of 0.0700%. When Eu_2SmSbO_7 was used as the photocatalyst, the conversion rate of chlorpyrifos was 88.16%, with a reaction rate of 2.94×10^{-9} mol·L^{-1}·s^{-1} and a photonic efficiency of 0.0617%. The conversion rate of chlorpyrifos that was derived from pesticide wastewater with $ZnBiEuO_4$ as the photocatalyst was 84.03%; at the same time, the reaction rate of 2.80×10^{-9} mol·L^{-1}·s^{-1} and the photonic efficiency of 0.0588% were achieved. When N-doped TiO_2 was used as the photocatalyst, the conversion rate of chlorpyrifos was 35.25%, with a reaction rate of 1.18×10^{-9} mol·L^{-1}·s^{-1} and a photonic efficiency of 0.0247%. Finally, when chlorpyrifos was photodegraded directly under VLID without the addition of any catalysts, the conversion rate of chlorpyrifos was 4.72%, with a reaction rate of 0.16×10^{-9} mol·L^{-1}·s^{-1} and a photonic efficiency of 0.0033%.

According to the above findings, it could be concluded that the descending order of photodegradation efficiency was as following: EZHP > Eu_2SmSbO_7 > $ZnBiEuO_4$ > N-doped TiO_2 under the same conditions. Comparing the conversion rates of chlorpyrifos after VLID of 160 min, it could be found that the conversion rate of chlorpyrifos using EZHP was 1.13 times higher than that with Eu_2SmSbO_7 as the photocatalyst, 1.19 times higher than that with $ZnBiEuO_4$ as the photocatalyst, and 2.84 times higher than that with N-doped TiO_2 as the photocatalyst.

Figure 16b presents the concentration variation curves of total organic carbon (TOC) during the photocatalytic degradation of chlorpyrifos within pesticide wastewater under VLID using EZHP, Eu_2SmSbO_7, $ZnBiEuO_4$, N-doped TiO_2, or without a catalyst. As can be seen from Figure 16b, the concentration of TOC decreased gradually with increasing VLID time.

By analyzing the data that are shown in Figure 16b, it was demonstrated that after VLID of 160 min, the conversion rates of TOC that was derived from pesticide wastewater were 98.02%, 84.04%, 80.12%, 30.23%, and 4.14% when chlorpyrifos was degraded using EZHP, Eu_2SmSbO_7, $ZnBiEuO_4$, N-doped TiO_2, or without catalyst, respectively. In other words, the descending order of the conversion rates of TOC during the degradation of chlorpyrifos was as follows: EZHP > Eu_2SmSbO_7 > $ZnBiEuO_4$ > N-doped TiO_2. The above results indicated that EZHP had a higher mineralization rate compared with Eu_2SmSbO_7, $ZnBiEuO_4$, or N-doped TiO_2 during the degradation of chlorpyrifos.

Figure 17 demonstrates the effect of different photocatalyst doses on the conversion rates when using EZHP to degrade chlorpyrifos under VLID. Beginning with the increase in the initial concentration of EZHP, the conversion rates of chlorpyrifos increased after VLID of 160 min. The conversion rate of chlorpyrifos reached 100% at an initial concentration of EZHP of 0.75 g/L. After that, the conversion rates of chlorpyrifos decreased with the increase in the initial concentration of EZHP. The reason for the decrease in the conversion rates of chlorpyrifos could be the aggregation of a high concentration of EZHP, which resulted in the decrease in active sites on the surface of the catalyst [101]. The above results indicated that the optimum conversion rate was achieved at an initial EZHP concentration of 0.75 g/L. Table 3 demonstrates the effect of different ratios of different catalysts to chlorpyrifos on the conversion rates of chlorpyrifos. From the data in Table 3, it can be seen that the optimum conversion rate of chlorpyrifos was achieved at a ratio of catalyst to chlorpyrifos of 66.96.

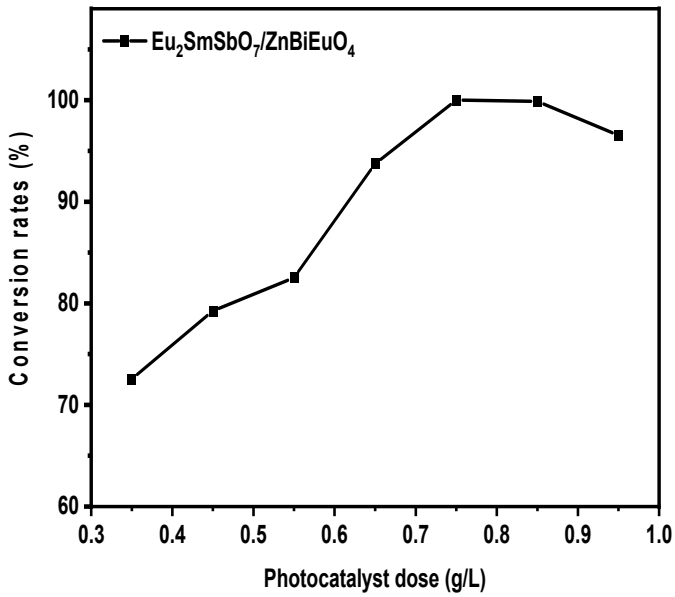

Figure 17. Effect of different photocatalyst doses on degradation of chlorpyrifos using EZHP under VLID.

Table 3. The effect of different ratios of catalyst to chlorpyrifos on conversion rates of chlorpyrifos.

Photocatalyst	Ratio of Catalyst to Chlorpyrifos	Conversion Rates of Chlorpyrifos (%)
$Eu_2SmSbO_7/ZnBiEuO_4$	31.25	72.56
	40.18	79.26
	49.11	82.52
	58.04	93.75
	66.96	100
	75.89	99.87
	84.82	96.54

The concentration variation curves of chlorpyrifos during four cyclic degradation experiments using EZHP under VLID are shown in Figure 18a. It can be deduced from Figure 18a that after VLID of 160 min using EZHP, the conversion rates of chlorpyrifos reached 98.16%, 97.03%, 96.03%, or 95.06%, respectively. From the four cyclic degradation experiments, the corresponding photon efficiencies were 0.0687%, 0.0679%, 0.0672%, or 0.0666%, respectively. Figure 18b illustrates the concentration variation curves of TOC during the photocatalytic degradation of chlorpyrifos using EZHP under VLID. It can be concluded from Figure 18b that the conversion rates of TOC were 96.94%, 95.72%, 94.68%, or 93.66% using EZHP after VLID of 160 min. According to the four consecutive cyclic degradation experiments using EZHP, the conversion rates of chlorpyrifos decreased by 1.84%, 1.13%, 1%, or 0.97% after each cyclic degradation experiment, respectively. It can be concluded from Figure 18b that the conversion rates of TOC decreased by 1.08%, 1.22%, 1.04%, or 1.02% after each cyclic degradation experiment using EZHP under VLID. The above results demonstrated that EZHP had excellent structural stability and reusability.

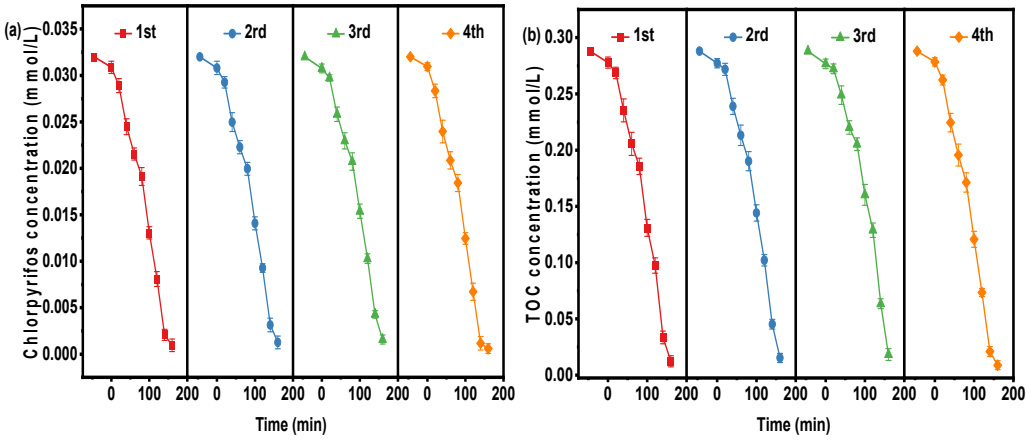

Figure 18. Concentration variation curves of (**a**) chlorpyrifos and (**b**) TOC during four cyclic degradation tests of chlorpyrifos that was derived from pesticide wastewater under VLID using EZHP.

To demonstrate the significance of our study in the field of photocatalytic degradation of chlorpyrifos, a comparative overview of relevant studies in this field is presented in Table 4. The data in Table 4 show that the photocatalytic activity of EZHP was better than that of other catalysts. These results indicate that EZHP can increase the conversion rates of chlorpyrifos and make a significant contribution to the field of photocatalysis. In conclusion, XRD and XPS analyses demonstrated the excellent structural stability of EZHP during the photocatalytic degradation of chlorpyrifos under VLID.

Table 4. Comparison of the photocatalytic activity of EZHP with that of other reported photocatalysts during photocatalytic degradation of chlorpyrifos.

Photocatalyst	Radiation	Irradiation Time (min)	Pesticide	Conversion Rates (%)	Ref.
TiO_2/H_2O_2	UV	300	Chlorpyrifos	70	[102]
Hollow TiO_2	UV	180	Chlorpyrifos	75.21	[103]
Cu/ZnO	Solar light	240	Chlorpyrifos	81	[61]
TiO_2/H_2O_2	Solar light	300	Chlorpyrifos	83	[102]
$CuS/Bi_2O_2CO_3$	Visible light	180	Chlorpyrifos	>95	[104]
CuO/TiO_2	Visible light	90	Chlorpyrifos	60	[105]
Ni-doped ZnO/TiO_2	Visible light	140	Chlorpyrifos	75.5	[106]
Eu_2SmSbO_7	Visible light	160	Chlorpyrifos	88.16	This study
EZHP	Visible light	160	Chlorpyrifos	100	This study

The first-order kinetic plots that correspond to chlorpyrifos concentration and VLID time during photocatalytic degradation of chlorpyrifos under VLID using EZHP, Eu_2SmSbO_7,

$ZnBiEuO_4$, N-doped TiO_2, or without a catalyst, are shown in Figure 19a. Figure 19b presents the first-order kinetic curves that correspond to TOC concentration and VLID time during photocatalytic degradation of chlorpyrifos under VLID using EZHP, Eu_2SmSbO_7, $ZnBiEuO_4$, N-doped TiO_2, or without a catalyst. The kinetic constants were calculated from the equation $\left(ln\frac{C_0}{C} = k_C t\right)$ and $\left(ln\frac{TOC_0}{TOC} = k_{TOC} t\right)$. In the equation, C_0 is the initial saturation of chlorpyrifos, C is the reactive saturation of chlorpyrifos, TOC_0 represents the initial saturation of total organic carbon, and TOC represents the reactive saturation of total organic carbon. It can be concluded from Figure 19a that the kinetic constant value K_C that was derived from the dynamic curves for EZHP, Eu_2SmSbO_7, $ZnBiEuO_4$, N-doped TiO_2, or without a catalyst, was 0.0202 min^{-1}, 0.0090 min^{-1}, 0.0075 min^{-1}, 0.0020 min^{-1}, and 0.0003 min^{-1} under VLID, and its corresponding linear correlation coefficient (R^2) was 0.8511, 0.8741, 0.8524, 0.9919, and 0.9773, respectively. Moreover, it can be deduced from Figure 19b that the kinetic constant value K_{TOC} that originated from the dynamic curves for EZHP, Eu_2SmSbO_7, $ZnBiEuO_4$, N-doped TiO_2, or without a catalyst, was 0.0182 min^{-1}, 0.0078 min^{-1}, 0.0067 min^{-1}, 0.0017 min^{-1}, and 0.0002 min^{-1} under VLID, and its corresponding R^2 was 0.8512, 0.8775, 0.8562, 0.9962, and 0.9745, respectively. According to the above studies, it was found that the mineralization efficiency during photocatalytic degradation of chlorpyrifos using EZHP was higher than that using Eu_2SmSbO_7 or $ZnBiEuO_4$ under VLID. Furthermore, the K_{TOC} value of the above four photocatalysts was lower than the K_C value of the above four photocatalysts, which indicates that the intermediate products might be formed during the photocatalytic degradation of chlorpyrifos.

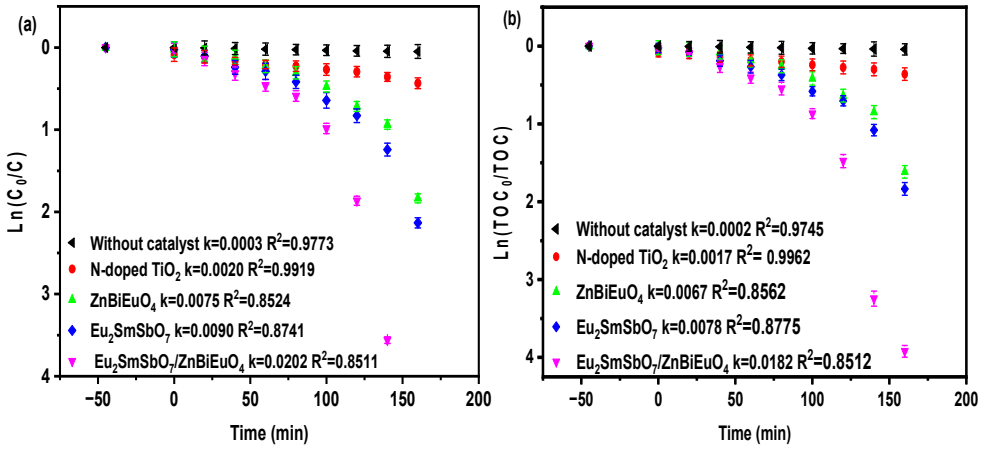

Figure 19. First-order kinetic plots of (**a**) chlorpyrifos and (**b**) TOC that were observed during photodegradation of chlorpyrifos under VLID using EZHP, Eu_2SmSbO_7, $ZnBiEuO_4$, N-doped TiO_2, or without a catalyst.

Figure 20a displays the first-order kinetic plots that correspond to chlorpyrifos concentration and VLID time during four cyclic degradation experiments for photocatalytic degradation of chlorpyrifos using EZHP. Figure 20b shows the first-order kinetic plots that correspond to TOC concentration and VLID time during four cyclic degradation experiments for photocatalytic degradation of chlorpyrifos using EZHP. Based on the analysis of the data in Figure 20a, the kinetic constant value K_C that was derived from the dynamic curves using EZHP for the four cyclic degradation experiments was 0.0186 min^{-1}, 0.0161 min^{-1}, 0.0144 min^{-1}, and 0.0131 min^{-1} under VLID, and its corresponding R^2 was 0.8527, 0.8605, 0.8604, and 0.8562, respectively. It can be deduced from Figure 20b that the kinetic constant value K_{TOC} that originated from the dynamic curves using EZHP for the four cyclic degradation experiments was 0.0158 min^{-1}, 0.0137 min^{-1}, 0.0125 min^{-1}, and 0.0110 min^{-1} under VLID, and its corresponding R^2 was 0.8608, 0.8517, 0.8509, and 0.8503, respectively. During the cycling experiments for degrading chlorpyrifos, we used the catalyst that was extracted from the previous degradation experiment of chlorpyrifos

for the next degradation experiment of chlorpyrifos; as a result, K_C and K_{TOC} decreased with the increasing number of cycling experiments. According to the above results, it could be concluded that the photocatalytic degradation of chlorpyrifos that was derived from pesticide wastewater using EZHP followed the first-order reaction kinetics under VLID.

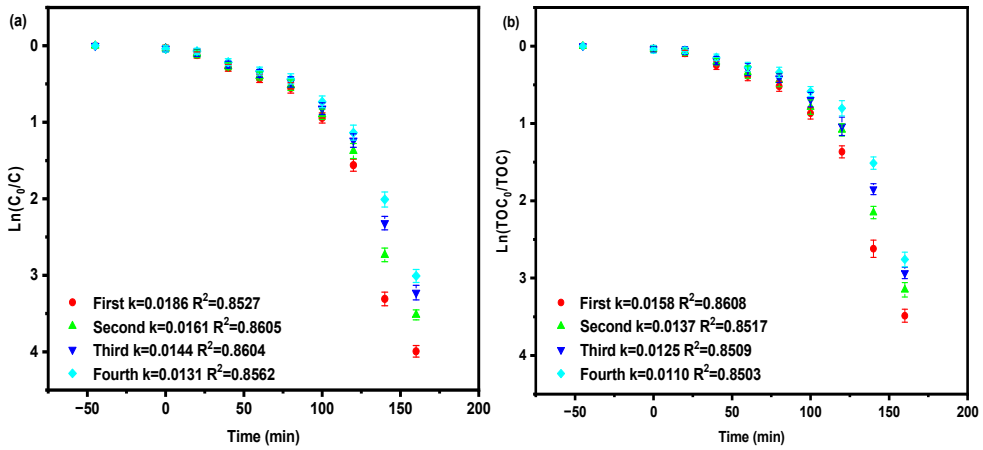

Figure 20. First-order kinetic plots of (**a**) chlorpyrifos and (**b**) TOC that were observed during four cyclic photodegradation experiments for chlorpyrifos under VLID using EZHP.

Figure 21 shows the XRD pattern of EZHP before and after the photocatalytic degradation reaction of chlorpyrifos. The crystal structure of EZHP before and after the photocatalytic degradation of chlorpyrifos under VLID did not change significantly, as can be seen in Figure 21. Figure 22 displays the XPS spectra of EZHP before and after the photocatalytic degradation reaction of chlorpyrifos. From Figure 22, it can be seen that the elemental composition and atomic valence of EZHP did not change remarkably before and after the photocatalytic degradation of chlorpyrifos under VLID.

Figure 23a shows the effect of different pH values on the conversion rates of chlorpyrifos during photocatalytic degradation of chlorpyrifos using EZHP under VLID. Analysis of the data in Figure 23a showed that the conversion rates of chlorpyrifos reached 99.2%, 100%, and 98.8% after VLID of 160 min at pH 3, 7, and 11, respectively. Therefore, it could be concluded that different pH values have little effect on the conversion rates of chlorpyrifos using EZHP under VLID.

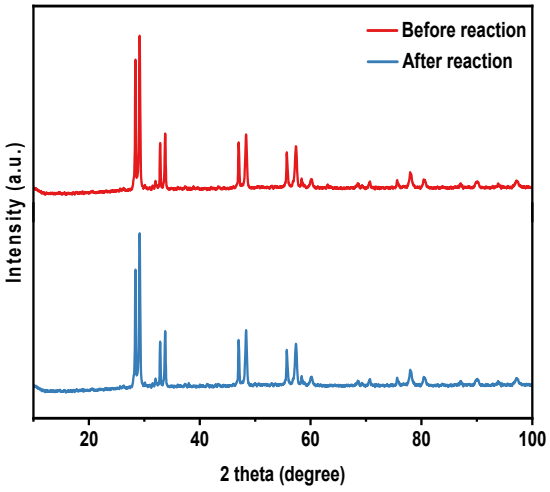

Figure 21. The XRD pattern of EZHP before photocatalytic degradation reaction of chlorpyrifos (red line), and the XRD pattern of EZHP after photocatalytic degradation reaction of chlorpyrifos (blue line).

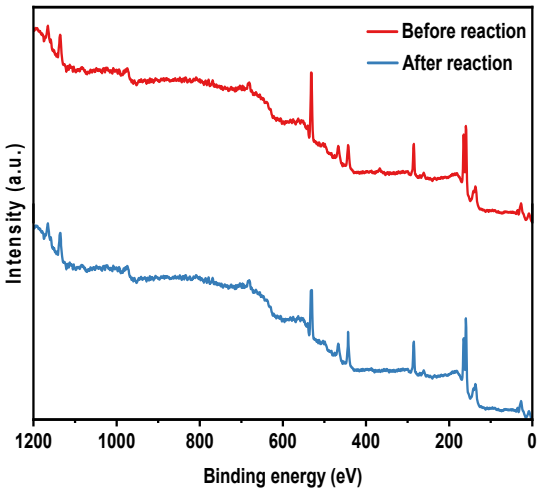

Figure 22. The XPS spectrum of EZHP before photocatalytic degradation reaction of chlorpyrifos (red line), and the XPS spectrum of EZHP after photocatalytic degradation reaction of chlorpyrifos (blue line).

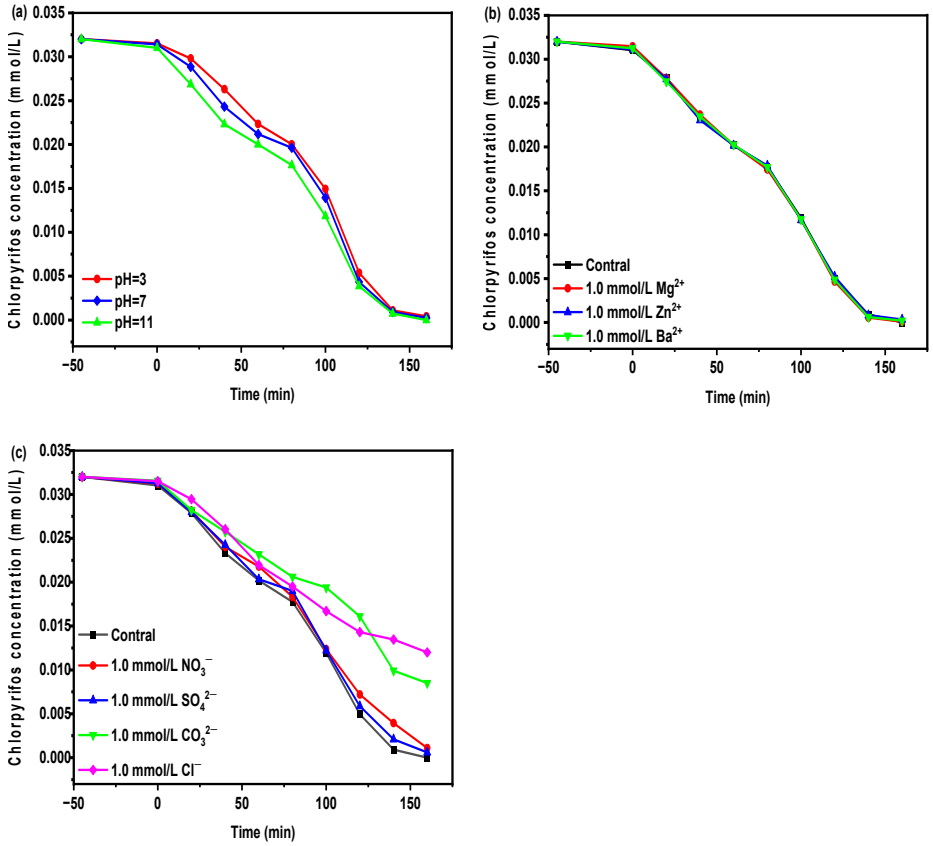

Figure 23. The effect of different (**a**) pH values, (**b**) metal ion species, and (**c**) anion species on the degradation of chlorpyrifos using EZHP under VLID.

Figure 23b displays the effect of different metal ions species on the conversion rates of chlorpyrifos during photocatalytic degradation of chlorpyrifos using EZHP under VLID. Ultrapure water containing Mg^{2+}, Zn^{2+}, or Ba^{2+} was introduced into the photocatalytic reaction system. It was found that the concentration of chlorpyrifos in pesticide wastewater decreased gradually with the increase in VLID time. In addition, by analyzing the data in Figure 23b, it could be seen that the conversion rate of chlorpyrifos using EZHP without the addition of metal ions after VLID of 160 min was 100%. Under the same conditions, the

introduction of 1 mmol/L Mg^{2+}, 1 mmol/L Zn^{2+}, or 1 mmol/L Ba^{2+} metal ions resulted in the conversion rates of chlorpyrifos to 99.75%, 98.94%, and 99.37%, respectively. Overall, the addition of Mg^{2+}, Zn^{2+}, or Ba^{2+} metal ions did not significantly inhibit the photocatalytic degradation of chlorpyrifos using EZHP under VLID.

Figure 23c presents the effect of different anion species on the conversion rates of chlorpyrifos during photocatalytic degradation of chlorpyrifos using EZHP under VLID. Ultrapure water containing NO_3^-, SO_4^{2-}, CO_3^{2-}, or Cl^- was introduced into the photocatalytic reaction system. It was found that the concentration of chlorpyrifos in pesticide wastewater decreased gradually with the increase of VLID time. Furthermore, by analyzing the data in Figure 23c, it could be seen that the conversion rate of chlorpyrifos using EZHP without the addition of anions after VLID of 160 min was 100%. Under the same conditions, the introduction of 1 mmol/L NO_3^-, 1 mmol/L SO_4^{2-}, 1 mmol/L CO_3^{2-}, or 1 mmol/L Cl^- anions resulted in the conversion rates of chlorpyrifos of 96.56%, 98.13%, 73.44%, and 62.50%, respectively. The Cl^- ion has a stronger inhibitory effect on the degradation of chlorpyrifos. The Cl^- ion consumes •OH and photo-induced holes, leading to the reduction of free radicals and thus hindering the photocatalytic reaction. The inhibition of chlorpyrifos degradation by NO_3^- or SO_4^{2-} ions was small. This is due to the fact that NO_3^- or SO_4^{2-} only consume the photo-induced holes in the photocatalytic reaction system, and thus the inhibition is weaker.

Figure 24 shows the effect of the addition of isopropanol (IPA), benzoquinone (BQ), or ethylenediaminetetraacetic acid (EDTA) on the conversion rates of chlorpyrifos using EZHP under VLID. In order to identify the active species involved in the photocatalytic reaction during chlorpyrifos photocatalytic degradation, different radical scavengers, as described above, were introduced at the beginning of the photocatalytic experiments. IPA captured hydroxyl radicals (•OH), while BQ captured superoxide anions ($\bullet O_2^-$) and EDTA captured holes (h^+). The volume of IPA, BQ, or EDTA added was 1 mL at a concentration of 0.15 mmol L^{-1}. Compared with the control group, the conversion rates of chlorpyrifos in the presence of IPA, BQ, or EDTA decreased by 47.62%, 35.66%, and 22.97% after VLID of 160 min. Therefore, it could be concluded that •OH, h^+, and $\bullet O_2^-$ acted as reactive radicals during the photocatalytic degradation of chlorpyrifos. The above experiments with the addition of scavengers showed that the oxidative removal capacities that were from the largest to the smallest for the three above oxidizing radicals during photocatalytic degrading of chlorpyrifos obeyed the following order: •OH > $\bullet O_2^-$ > h^+. Thus, we could conclude that •OH possessed the strongest oxidative removal ability for photocatalytic degradation of chlorpyrifos within pesticide wastewater.

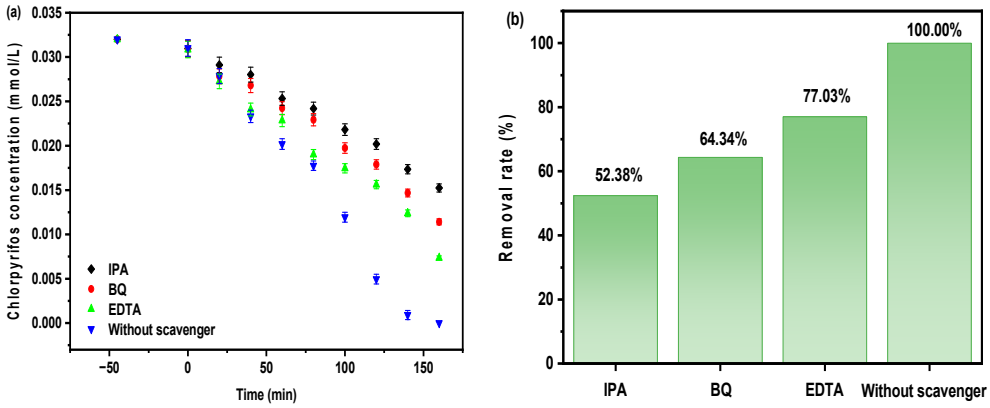

Figure 24. (**a**) Effect of different scavengers such as BQ, IPA, or EDTA on removal efficiency of chlorpyrifos using EZHP under VLID; (**b**) effect of different scavengers on chlorpyrifos conversion rates during photocatalytic degradation of chlorpyrifos using EZHP under VLID.

Photoluminescence (PL) spectra and time-resolved photoluminescence (TRPL) spectra can reflect the complexation rate of photo-induced electrons and photo-induced holes,

and provide the electronic lifetime of the photocatalyst. Figure 25a displays the PL spectra of EZHP, Eu_2SmSbO_7, and $ZnBiEuO_4$. Figure 25b–d show the TRPL spectrum of Eu_2SmSbO_7, $ZnBiEuO_4$, and EZHP, respectively. The lower the relative intensities of the vertical coordinates corresponding to the PL spectra, the more difficult it was to combine the photo-induced electrons and photo-induced holes. The above results would lead to the prolongation of the survival life of photo-induced electrons and photo-induced holes; as a result, the numbers of $\bullet O_2^-$ and •OH would be increased. Ultimately, the photocatalytic activity was improved [107,108]. According to Figure 25a, it can be seen that the value of the relative intensity of the longitudinal coordinate of the PL spectrum corresponding to EZHP was lower than the value of the relative intensity of the longitudinal coordinate of the PL spectrogram corresponding to Eu_2SmSbO_7. At the same time, the value of the relative intensity of the longitudinal coordinate of the PL spectrum corresponding to Eu_2SmSbO_7 was lower than the value of the relative intensity of the longitudinal coordinate of the PL spectrum corresponding to $ZnBiEuO_4$. Therefore, based on above results, it could be concluded that the photocatalytic activity was ranked from high to low as follows: EZHP > Eu_2SmSbO_7 > $ZnBiEuO_4$. The above results suggest that the compounding rate of the photo-induced electrons and the photo-induced holes could be reduced by constructing a heterojunction structure. The TRPL spectrum of Eu_2SmSbO_7, $ZnBiEuO_4$, and EZHP in Figure 25b–d was fitted by the double-exponential decay shown in Equation (4) [109]:

$$I(t) = I_0 + A_1\, exp\left(-\frac{t}{\tau_1}\right) + A_2\, exp\left(-\frac{t}{\tau_2}\right) \quad (4)$$

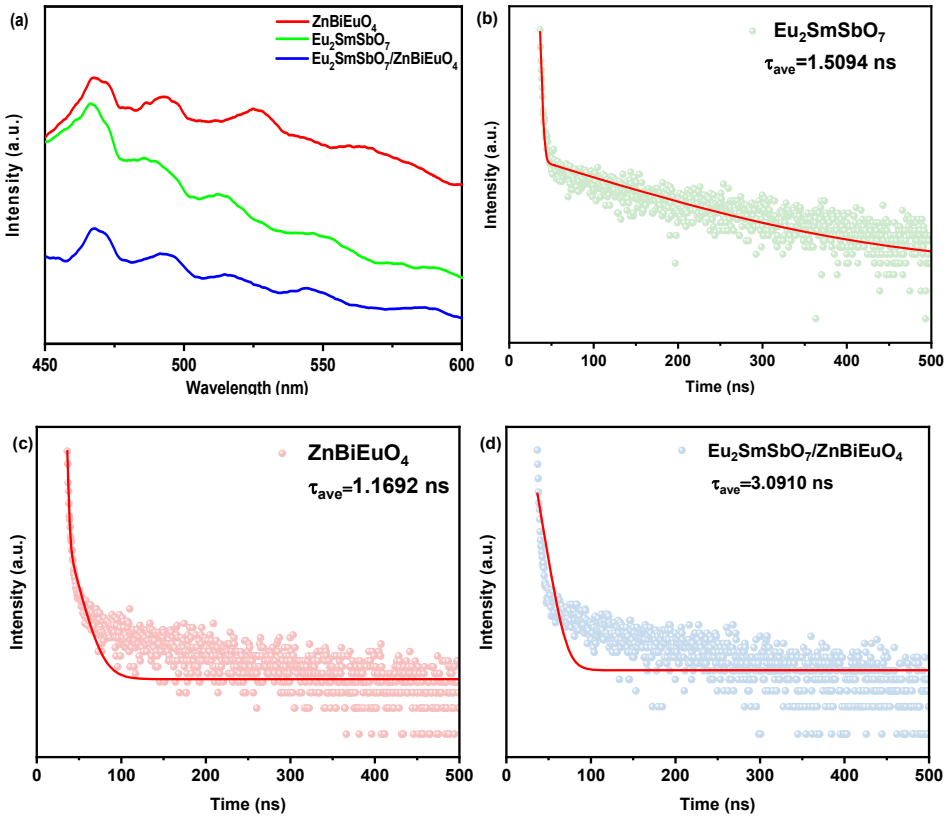

Figure 25. (**a**) PL spectra of EZHP, Eu_2SmSbO_7, and $ZnBiEuO_4$, and TRPL spectra of (**b**) Eu_2SmSbO_7, (**c**) $ZnBiEuO_4$, (**d**) and EZHP (red line: curves generated by nonlinear curve fitting).

In above equations, τ_1 or τ_2 denote the fast and slow attenuation components, respectively. It is usually assumed that the τ_1 component is attributed to non-radiative recombination involving defects or traps, while the τ_2 component corresponds to radiative

recombination within the photocatalyst. In order to obtain the average electron lifetime (τ_{ave}), Equation (5) could be used as follows [110]:

$$\tau_{ave} = \left(A_1\tau_1^2 + A_2\tau_2^2\right)/(A_1\tau_1 + A_2\tau_2) \quad (5)$$

Table 5 lists the calculated lifetimes and the corresponding parameters. By comparing the data in Table 5, it was observed that the average electron lifetime of EZHP (τ_{ave} = 3.0910 ns) was higher than the average electron lifetime of Eu_2SmSbO_7 (τ_{ave} = 1.5094 ns) and the average electron lifetime of $ZnBiEuO_4$ (τ_{ave} = 1.1692 ns). The above results again indicate that EZHP had a better photocatalytic activity than Eu_2SmSbO_7 or $ZnBiEuO_4$.

Table 5. Fitted results of TRPL curves of Eu_2SmSbO_7, $ZnBiEuO_4$, and EZHP.

	Eu_2SmSbO_7	$ZnBiEuO_4$	$Eu_2SmSbO_7/ZnBiEuO_4$
A_1	3.1295×10^{10}	2.4041×10^{13}	39.4378
τ_1 (ns)	1.5094	1.1692	7.6479
A_2	0.0455	2.2526	811.5324
τ_2 (ns)	140.8084	11.1017	2.3793
τ_{ave} (ns)	1.5094	1.1692	3.0910

Electrochemical impedance spectroscopy (EIS) reflects the relationship between the impedance of the electrode interface and the frequency of the change in the applied voltage or current under light conditions. At the same time, the migration process of photo-induced electrons and photo-induced holes at the interfaces of Eu_2SmSbO_7 and $ZnBiEuO_4$, which constituted the EZHP, could be understood based on the EIS. The radius of the arc in the Nyquist impedance diagram can be used to compare the compounding rates of photo-induced electrons and photo-induced holes in the catalysts; thus, the length of the survival lifetimes of the photo-induced electrons and photo-induced holes can be determined. Figure 26 illustrates the Nyquist impedance plot of EZHP, Eu_2SmSbO_7, and $ZnBiEuO_4$. It should be known that the smaller the arc radius of the Nyquist impedance plots profile of the catalyst, the more difficult it was to combine the photo-induced electrons and photo-induced holes, which led to the longer survival life of the photo-induced electrons and photo-induced holes [67]. As can be seen from Figure 26, the descending order of the arc radius that was derived from the Nyquist impedance plot was as follows: $ZnBiEuO_4$ > Eu_2SmSbO_7 > EZHP. The above results show that the prepared EZHP had a longer survival lifetime of photo-induced electrons and photo-induced holes and higher interfacial charge mobility; thus, EZHP had better photocatalytic activity.

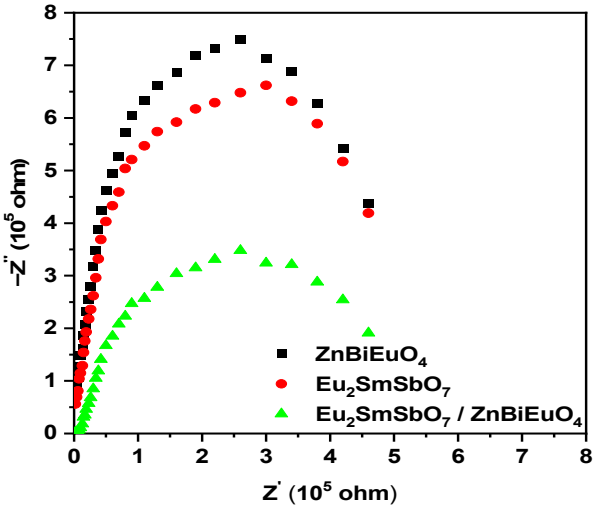

Figure 26. Nyquist impedance plots of EZHP, Eu_2SmSbO_7 photocatalyst, and $ZnBiEuO_4$ photocatalyst.

2.8. Analysis of Possible Degradation Mechanisms

The conceivable photocatalytic degradation mechanism of chlorpyrifos using EZHP under VLID is illustrated in Figure 27. The electrochemical potential of the conduction band (CB) in semiconductor catalysts could be calculated according to Equation (6) [111]. According to Equation (7), the electrochemical potential of the valence band (VB) in the semiconductor catalyst could be calculated [111]. Equations (6) and (7) are as follows:

$$E_{CB} = X - E^e - 0.5E_g \tag{6}$$

$$E_{VB} = E_{CB} + E_g \tag{7}$$

where E_g is the band gap of the semiconductor and E^e is the energy of the free electrons on the hydrogen scale (about 4.5 eV). X is the electronegativity of the semiconductor. X is the average of the ionization energy (I) and the electron affinity energy (A), expressed through Equation (8) [112]. The X of the photocatalyst could be calculated using Equation (9) [113].

$$X = (I + A)/2 \tag{8}$$

$$X = \left[X(A)^a X(B)^b X(C)^c\right]^{1/(a+b+c)} \tag{9}$$

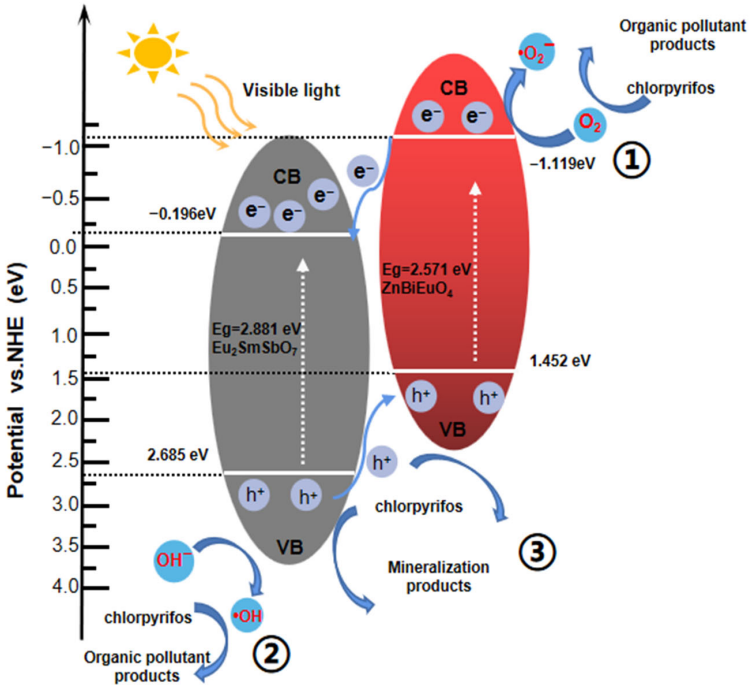

Figure 27. Possible photocatalytic degradation mechanism of degradation using EZHP under VLID (1, 2, and 3: the three degradation pathways of chlorpyrifos).

A, *B*, and *C* and *a*, *b*, and *c* are the corresponding element and atomic numbers in the semiconductor photocatalysts. The electronegativity of Eu_2SmSbO_7 and $ZnBiEuO_4$ was calculated to be 5.745 and 4.667, respectively. Based on above equations, the VB potential and CB potential of Eu_2SmSbO_7 were estimated to be 2.685 eV and −0.196 eV, respectively; contemporaneously, the VB potential and CB potential of $ZnBiEuO_4$ were estimated to be 1.452 eV and −1.119 eV, respectively. Eu_2SmSbO_7 and $ZnBiEuO_4$ were both able to absorb visible light energy and produced electron–hole pairs when Eu_2SmSbO_7 or $ZnBiEuO_4$ was exposed to VLID. The redox potential of the CB for $ZnBiEuO_4$ (−1.119 eV) was more negative than the redox potential of the CB for Eu_2SmSbO_7 (−0.196 eV). At the same

time, the redox potential position of the VB of Eu_2SmSbO_7 (2.685 eV) was more positive than the redox potential position of the VB for $ZnBiEuO_4$ (1.452 eV). Therefore, the photo-induced electrons on the CB of $ZnBiEuO_4$ could be transferred to the CB of Eu_2SmSbO_7, while the photo-induced holes on the VB of Eu_2SmSbO_7 could be transferred to the VB of $ZnBiEuO_4$. Therefore, the composition of EZHP effectively increased the separation rate of photo-induced electrons and photo-induced holes; as a result, the above results improved the interfacial charge transfer efficiency [114]. More oxidizing radicals (•OH and $•O_2^-$) participated during the photocatalytic reaction process of degrading chlorpyrifos, thereby improving the degradation efficiency.

In addition, as shown in pathway 1 of Figure 27, because the CB potential of $ZnBiEuO_4$ (−1.119 eV) was more negative than the potential of $O_2/•O_2^-$ (−0.33 eV), the photo-induced electrons within the CB of $ZnBiEuO_4$ could absorb oxygen to produce $•O_2^-$. $•O_2^-$ was used to degrade chlorpyrifos. Similarly, as illustrated in pathway 2 of Figure 27, because the VB potential of Eu_2SmSbO_7 (2.685 eV) was more positive than the potential of $OH^-/•OH$ (2.38 eV), the photo-induced holes in the VB of Eu_2SmSbO_7 could oxidize H_2O or OH^- into •OH, which could degrade chlorpyrifos. Finally, the photo-induced holes within the VB of $ZnBiEuO_4$ or Eu_2SmSbO_7 could directly oxidize chlorpyrifos, as illustrated in Path 3 of Figure 27. In conclusion, the construction of EZHP could enhance the separation rate of the photo-induced electrons and the photo-induced holes; therefore, EZHP exhibited excellent photocatalytic performance during the process of degrading chlorpyrifos.

The basic principle of the ultraviolet photoelectron spectroscopy (UPS) is the photoelectric effect, with ultraviolet light as the excitation light source. The ionization potential of the photocatalyst and the electrochemical potential of the VB could be obtained by UPS. The UPS spectrum of Eu_2SmSbO_7 is illustrated in Figure 28a. It can be deduced from Figure 28a that the measured onset (Ei) energy and cut-off (Ecutoff) energy of Eu_2SmSbO_7 were 0.496 eV and 19.011 eV, respectively. Figure 28b presents the UPS spectrum of $ZnBiEuO_4$. It can be deduced from Figure 28b that the onset (Ei) energy and cut-off (Ecutoff) energy of $ZnBiEuO_4$ were measured to be 0.159 eV and 19.907 eV, respectively. The ionization potentials of Eu_2SmSbO_7 and $ZnBiEuO_4$ could be calculated by decreasing the width of the UPS spectrum by the excitation energy, which was about 21.2 eV [115]. According to the above approach, the VB ionization potential of Eu_2SmSbO_7 and $ZnBiEuO_4$ was calculated to be 2.685 eV and 1.452 eV, respectively, which was consistent with the VB potential that was derived from the above simulation calculation results.

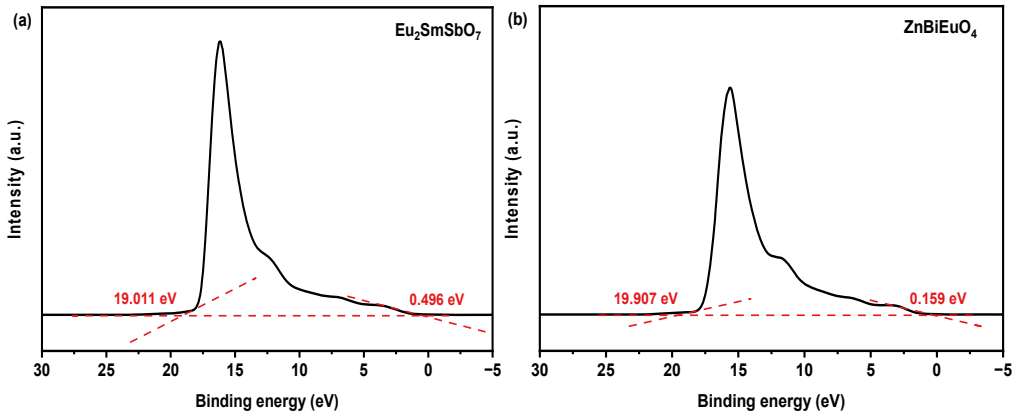

Figure 28. Ultraviolet photoelectron spectrum (UPS) of (**a**) Eu_2SmSbO_7 and (**b**) $ZnBiEuO_4$.

The electrochemical potential of $O_2/•O^{2-}$ was -0.33 eV and the absolute electrochemical potential value of $OH^-/•OH$ was 2.38 eV. The ionization potentials of the VB for Eu_2SmSbO_7 and $ZnBiEuO_4$ were calculated to be 2.685 eV and 1.452 eV, respectively. Thus, it can be deduced from Figure 28 that the photo-induced holes in the VB of Eu_2SmSbO_7 possessed the ability to oxidize H_2O or OH^- to form •OH. In addition, the CB potential of Eu_2SmSbO_7 and $ZnBiEuO_4$ was −0.196 eV and −1.119 eV, respectively, which indicated

that the photo-induced electrons in the conduction band of $ZnBiEuO_4$ could absorb O_2 to form $\bullet O_2^-$.

Based on above studies, EZHP possessed the ability to produce •OH and $\bullet O_2^-$ under VLID, which could degrade chlorpyrifos efficiently within pesticide wastewater.

The intermediates produced during chlorpyrifos degradation by LC-MS were identified to investigate the mechanism of chlorpyrifos degradation. The intermediate products were identified as $C_5H_2Cl_3NO$ (m/z = 196), $C_5H_2Cl_3N$ (m/z = 180), $C_5H_3Cl_2NO$ (m/z = 162), $C_5H_3Cl_2N$ (m/z = 146), C_5H_5N (m/z = 79), $C_4H_{11}O_3PS$ (m/z = 170), $C_4H_{11}O_4P$ (m/z = 154), $C_2H_7O_4P$ (m/z = 126), and H_3O_4P (m/z = 97). Based on above-mentioned detected intermediate products, we could deduce the degradation pathway of chlorpyrifos. Figure 29 shows the degradation pathway of chlorpyrifos. From Figure 29, it can be seen that chlorpyrifos underwent oxidation and hydroxylation reactions during photocatalytic degradation. Eventually, the above results revealed that chlorpyrifos was converted to CO_2, H_2O, SO_4^{2-}, NO^{3-}, and PO_4^{3-}.

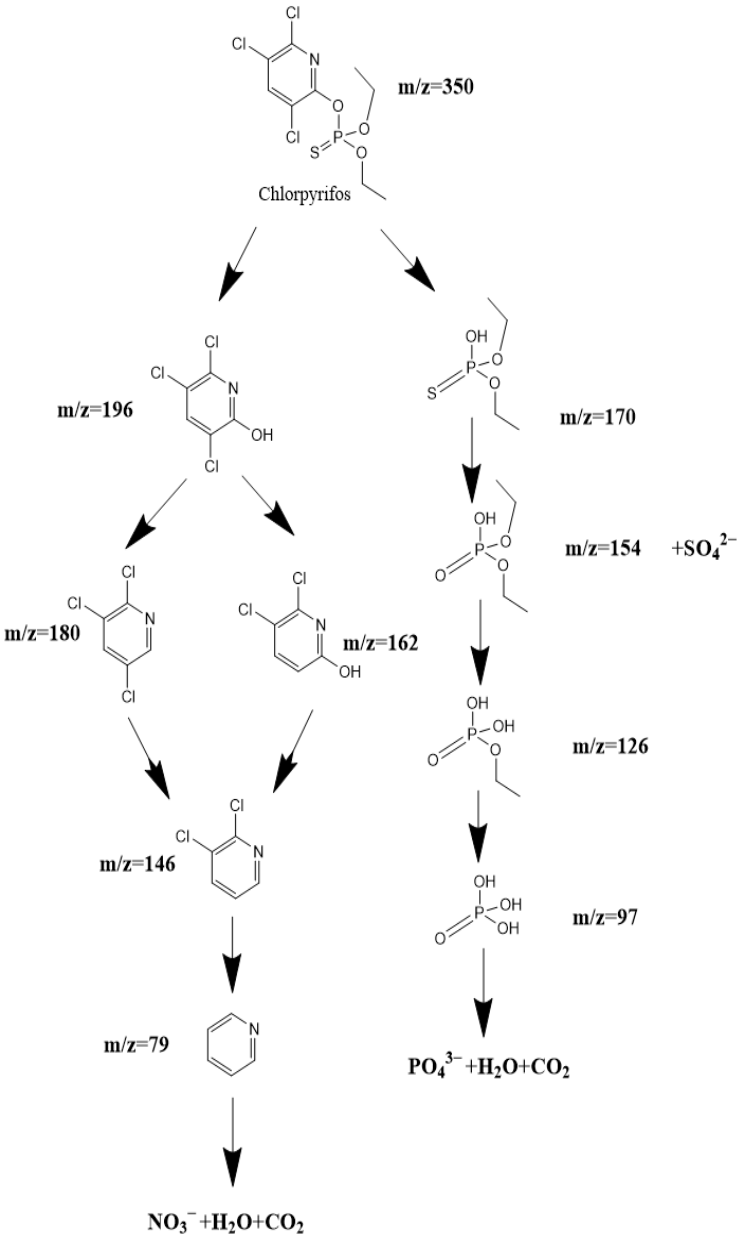

Figure 29. Suggested photocatalytic pathway scheme for the degradation of chlorpyrifos under VLID with EZ heterojunction as photocatalyst.

3. Experimental Section

3.1. Materials and Reagents

Materials purchased from Sinopharm Group Chemical Reagent Co., Ltd. (Shanghai, China) includes ethylenediaminetetraacetic acid (EDTA, $C_{10}H_{16}N_2O_8$, purity = 99.5%), isopropanol (IPA, C_3H_8O, purity $\geq$ 99.7%), and P-benzoquinone (BQ, $C_6H_4O_2$, purity $\geq$ 98.0%). Materials purchased from Aladdin Group Chemical Reagent Co., Ltd. (Shanghai, China) included $Eu(NO_3)_3{\cdot}6H_2O$ (purity = 99.99%), $Sm(NO_3)_3{\cdot}6H_2O$ (purity = 99.9%), $SbCl_5$ (purity = 99.99%), $Zn(NO_3)_2{\cdot}6H_2O$ (purity = 99.99%), $Bi(NO_3)_3{\cdot}5H_2O$ (purity = 99.99%) tetrabutyl titanate ($C_{16}H_{36}O_4Ti$, purity = 99.99%), ammonia (H_5NO, purity $\geq$ 25%), glacial acetic acid (CH_3CO_2H, purity = 100%), absolute ethanol (C_2H_5OH, purity $\geq$ 99.5%), and chlorpyrifos ($C_9H_{11}Cl_3NO_3PS$, purity $\geq$ 99.0%). Ultrapure water (18.25 MU cm) was used during the experiment.

3.2. Synthesis of N-Doped TiO_2

Nitrogen-doped titanium dioxide (N-doped TiO_2) used in this research was synthesized by the sol–gel method using tetrabutyl titanate as the precursor and ethanol as the dissolvent. N-doped TiO_2 was synthesized as follows:

In the first step, mixed Solution 1 (17 mL tetrabutyl titanate and 40 mL absolute ethanol) and mixed Solution 2 (5 mL double-distilled water, 10 mL glacial acetic acid, and 40 mL absolute ethanol) were prepared, and mixed Solution 1 was added to mixed Solution 2 by dropwise addition under continuous stirring. At this time, a transparent colloidal suspension was obtained. In the second step, ammonia (N/Ti ratio of 8 mol%) was added to the above solution to form a dry gel after 48 h of aging. Finally, the dry gel was ground into powder and calcined at 500 °C for 2 h and then ground again and passed through a vibrating sieve to obtain N-TiO_2 powder.

3.3. Synthesis of Eu_2SmSbO_7/$ZnBiEuO_4$ Heterojunction Photocatalyst

Eu_2SmSbO_7 and $ZnBiEuO_4$ were prepared by the hydrothermal method. Quantities of 0.30 mol/L $Eu(NO_3)_3{\cdot}6H_2O$, 0.15 mol/L $Sm(NO_3)_3{\cdot}6H_2O$, and 0.15 mol/L $SbCl_5$ were mixed and stirred for 20 h and then transferred to a Teflon-lined autoclave and heated at 200 °C for 15 h. Subsequently, the resulting powder was calcined in a tube furnace at 790 °C for 10 h under nitrogen to obtain Eu_2SmSbO_7 powder.

To prepare $ZnBiEuO_4$, 0.15 mol/L $Zn(NO_3)_2{\cdot}6H_2O$, 0.15 mol/L $Bi(NO_3)_3{\cdot}5H_2O$, and 0.15 mol/L $Eu(NO_3)_3{\cdot}6H_2O$ were mixed and stirred for 20 h. The solution was transferred to a Teflon-lined autoclave and heated at 200 °C for 15 h and then calcined in a tube furnace under nitrogen at 770 °C for 10 h.

In this study, the solvothermal method was used to synthesize EZHP. The synthesized Eu_2SmSbO_7 (1 mol) and $ZnBiEuO_4$ (1 mol) were added to 300 mL of octanol ($C_8H_{18}O$) and dispersed for 1 h using an ultrasonic wave. Then, in order to make it easier for $ZnBiEuO_4$ to adhere to the surface of Eu_2SmSbO_7, it was heated and refluxed at 150 v for 2 h under vigorous stirring. Finally, the product was collected by centrifugation after cooling to room temperature. The collected EZHP was washed several times with a hexane/ethanol mixture to purify the EZHP. The pure EZHP was dried at 60 °C for 6 h and stored.

3.4. Characterization

In order to analyze the properties such as the crystal structure of Eu_2SmSbO_7 and $ZnBiEuO_4$, the tests were carried out using an X-ray diffractometer (XRD, Shimadzu, XRD-6000, Kyoto, Japan). The conformation and microstructure of EZHP were characterized using a transmission electron microscope (TEM, JEM—F200 FEI Tecnai G2 F20 FEI Talos F200s, Thermo Fisher Scientific Corporation, Waltham, MA, USA), and the micro-regional compositional elements of the samples were determined using energy dispersive spectroscopy (EDS). To obtain the energy band widths of Eu_2SmSbO_7, $ZnBiEuO_4$, and EZHP, a UV–visible spectrophotometer (UV-Vis DRS, Shimadzu, UV-3600, Kyoto, Japan) was used. A Fourier transform infrared spectrometer (FTIR, WQF-530A, Beifen-Ruili Analytical

Instrument (Group) Co., Ltd., Beijing, China) and laser Raman spectrometer (INVIA0919-06, Renishaw plc New Mills Wotton-under-Edge Gloucestershire GL12 8JR, London, United Kingdom) were used to analyze the chemical bonding of Eu_2SmSbO_7, $ZnBiEuO_4$, and EZHP. The surface chemistry and valence states of Eu_2SmSbO_7, $ZnBiEuO_4$, and EZHP were analyzed using an X-ray photoelectron spectrometer (XPS, PHI 5000 VersaProbe, UlVAC-PHI, Chigasaki, Japan) and an Al-kα X-ray source. The ionization potentials of Eu_2SmSbO_7 and $ZnBiEuO_4$ were analyzed by Ultraviolet photoelectron spectroscopy (UPS, Escalab 250Xi, Thermo Fisher Scientific Corporation, Waltham, MA, USA).

3.5. Photoelectrochemical Experiments

The electrochemical impedance spectroscopy (EIS) of Eu_2SmSbO_7, $ZnBiEuO_4$, and EZHP was experimentally derived from a CHI660D electrochemical bench (Shanghai Zhenhua Instrument Co., Ltd., Shanghai, China) equipped with standard three electrodes. The working electrodes were fabricated by mixing 0.03 g of photocatalyst (Eu_2SmSbO_7, $ZnBiEuO_4$, or EZHP) and 0.01 g chitosan with 0.45 mL of dimethylformamide, and then ultrasonicated for 1 h. The processed solution was added dropwise to a conductive glass (10 mm $\times$ 20 mm) made with indium tin oxide (ITO) and then dried at 80 °C for 10 min. A platinum plate was used as the counter electrode and an Ag/AgCl electrode was used as the reference electrode. Na_2SO_4 aqueous solution (0.5 mol/L) was used as the electrolyte. A 500 W Xe lamp with a 420 nm cut-off filter was used as the experimental light source.

3.6. Experimental Setup and Procedure

The photocatalytic experiments were carried out at a constant temperature of 20 °C, and the visible light in the experiments was simulated using a xenon lamp (500 W) with a cut-off filter (420 nm) in a photochemistry chamber (CEL-LB70, China Education Au-Light Technology Co., Ltd., Beijing, China).

Twelve identical quartz tubes with a volume of 40 mL were used for the individual reaction solutions. The total reaction volume of the pesticide effluent was 480 mL. The amount of catalyst (Eu_2SmSbO_7 or $ZnBiEuO_4$) was 0.75 g/L. The amount of EZHP was 0.35 g/L, 0.45 g/L 0.55 g/L, 0.65 g/L 0.75 g/L, 0.85 g/L, or 0.95 g/L. The initial concentration of chlorpyrifos was 0.032 mmol/L.

The concentration of chlorpyrifos in the solution was determined by liquid chromatography (Agilent Technologies, Palo Alto, CA, USA) after filtering out the catalyst from 3 mL of the suspension at the corresponding time according to the experimental requirements. The mobile phase consisted of one-half CH_3CN and one-half distilled deionized water. The injection volume of the test solution was 10 μL, and the flow rate was 1 mL·min^{-1}.

In order to establish a reaction system with an equilibrium of adsorption/desorption of the photocatalyst, chlorpyrifos, and atmospheric oxygen, the solution containing the photocatalyst and chlorpyrifos was magnetically stirred for 45 min under dark conditions before VLID. Stirring was conducted at 500 rpm/min during the desorption of chlorpyrifos under VLID.

In order to determine the concentration of TOC during the photocatalytic degradation of chlorpyrifos, the solution was analyzed using a TOC analyzer (TOC-5000 A, Shimadzu Corporation, Kyoto, Japan). Potassium acid phthalate ($KHC_8H_4O_4$) solutions of known carbon concentration (0 to 100 mg/L) were prepared as standard reagents for comparison. The TOC concentration of six reaction solutions of 45 mL was measured.

A liquid chromatograph mass spectrometer (LC-MS, Thermo Quest LCQ Duo, Thermo Fisher Scientific Corporation, Waltham, MA, USA) was used to identify the intermediates produced during the photocatalytic degradation of chlorpyrifos. After the photocatalytic degradation of chlorpyrifos, 20 μL of the solution was automatically injected into the instrument for testing. The mobile phase consisted of 60% methanol and 40% ultrapure water at a flow rate of 0.2 mL/min. The relevant parameter conditions for the experiment were set to a capillary temperature of 27 °C, a voltage of 19.00 V, a spray voltage of 5000 V, and a constant sheath gas flow rate. The m/z range of the test spectrum was 50 to 600.

The incident photon flux I_o was 4.76 × 10^{-6} Einstein L^{-1} s^{-1} under VLID measured with a radiometer (Model FZ-A, Photoelectric Instrument Factory Beijing Normal University, Beijing, China). The incident photon flux could be adjusted by varying the distance between the photoreactor and the xenon arc lamp.

The photonic efficiency could be calculated by Equation (10):

$$\phi = \frac{R}{I_o} \tag{10}$$

In the above equations, ϕ, R, and I_o represent the photonic efficiency (%), conversion rate of chlorpyrifos (mol L^{-1} s^{-1}), and incident photon flux (Einstein L^{-1} s^{-1}), respectively.

4. Conclusions

In this study, Eu_2SmSbO_7 with high photocatalytic activity was prepared via the hydrothermal method for the first time. The new photocatalyst, Eu_2SmSbO_7, was proven to be a pure phase with a pyrochlore structure, cubic crystal system, and *Fd3m* space group. Various characterization techniques, such as XRD analysis, FT-IR, Raman spectrometry, UV-Vis, XPS, and TEM-EDS, were utilized to detect the properties of the newly prepared photocatalysts. The lattice parameter and band gap of Eu_2SmSbO_7 were a = 10.5547 Å and 2.881 eV, respectively. EZHP was successfully prepared using the solvothermal method for the first time. The results demonstrated that EZHP was effective for removing chlorpyrifos from pesticide wastewater. After VLID of 160 min to degrade chlorpyrifos using EZHP, the conversion rate of chlorpyrifos reached 100% and the conversion rate of TOC was 98.02%. The kinetic constant value K_C that was derived from the dynamic curves for EZHP was 0.0202 min^{-1}. After VLID of 160 min to degrade chlorpyrifos using Eu_2SmSbO_7, the conversion rate of chlorpyrifos reached 88.16% and the conversion rate of TOC was 84.04%. The kinetic constant value K_C that was derived from the dynamic curves for Eu_2SmSbO_7 was 0.0090 min^{-1}. After VLID of 160 min, the conversion rates of chlorpyrifos using EZHP were 1.13 times, 1.19 times, and 2.84 times higher than the conversion rates of chlorpyrifos with Eu_2SmSbO_7, $ZnBiEuO_4$, or N-doped TiO_2 as the photocatalyst. Therefore, it can be concluded that the use of EZHP was an effective method for treating chlorpyrifos that was derived from pesticide wastewater. Finally, the possible photodegradation pathways of chlorpyrifos was hypothesized. Chlorpyrifos was degraded into inorganic compounds such as CO_2, H_2O, SO_4^{2-}, NO^{3-}, and PO_4^{3-}.

Author Contributions: J.L. (Jingfei Luan): conceptualization, data curation, formal analysis, investigation, methodology, software, visualization, writing—original draft preparation, writing—review and editing, validation. Y.W.: software, data curation, methodology, writing—original draft preparation, validation. Y.Y.: formal analysis, investigation, writing—original draft preparation, validation, investigation. L.H.: software, visualization, validation. J.L. (Jun Li): formal analysis, methodology, writing—original draft preparation. Y.C.: software, validation, data curation. All authors have read and agreed to the published version of the manuscript.

Funding: This study was supported by the Free Exploring Key Item of the Natural Science Foundation of the Science and Technology Development Plan Project of Jilin Province, China (Grant No. YDZJ202101ZYTS161).

Data Availability Statement: Data are contained within the article.

Conflicts of Interest: There are no conflicts of interest to declare.

References

1. Soria-Lopez, A.; Garcia-Perez, P.; Carpena, M.; Garcia-Oliveira, P.; Otero, P.; Fraga-Corral, M.; Cao, H.; Prieto, M.A.; Simal-Gandara, J. Challenges for future food systems: From the Green Revolution to food supply chains with a special focus on sustainability. *Food Front.* **2023**, *4*, 9–20. [CrossRef]
2. Fukase, E.; Martin, W. Economic growth, convergence, and world food demand and supply. *World. Dev.* **2020**, *132*, 104954. [CrossRef]

3. Webb, R.; Buratini, J. Global Challenges for the 21st Century: The Role and Strategy of the Agri-Food Sector. *Anim. Reprod.* **2016**, *13*, 133–142. [CrossRef]
4. Liu, Y.B.; Pan, X.B.; Li, J.S. A 1961–2010 record of fertilizer use, pesticide application and cereal yields: A review. *Agron. Sustain. Dev.* **2015**, *35*, 83–93. [CrossRef]
5. Delcour, I.; Spanoghe, P.; Uyttendaele, M. Literature review: Impact of climate change on pesticide use. *Food Res. Int.* **2015**, *68*, 7–15. [CrossRef]
6. Popp, J.; Peto, K.; Nagy, J. Pesticide productivity and food security. A review. *Agron. Sustain. Dev.* **2013**, *33*, 243–255. [CrossRef]
7. Washuck, N.; Hanson, M.; Prosser, R. Yield to the data: Some perspective on crop productivity and pesticides. *Pest Manag. Sci.* **2022**, *78*, 1765–1771. [CrossRef]
8. Rodrigues, E.T.; Lopes, I.; Pardal, M.A. Occurrence, fate and effects of azoxystrobin in aquatic ecosystems: A review. *Environ. Int.* **2013**, *53*, 18–28. [CrossRef]
9. Wahab, S.; Muzammil, K.; Nasir, N.; Khan, M.S.; Ahmad, M.F.; Khalid, M.; Ahmad, W.; Dawria, A.; Reddy, L.K.V.; Busayli, A.M. Advancement and New Trends in Analysis of Pesticide Residues in Food: A Comprehensive Review. *Plants* **2022**, *11*, 1106. [CrossRef]
10. Wan, M.T. Ecological risk of pesticide residues in the British Columbia environment: 1973–2012. *J. Environ. Sci. Health B* **2013**, *48*, 344–363. [CrossRef]
11. El-Sheikh, E.S.A.; Ramadan, M.M.; El-Sobki, A.E.; Shalaby, A.A.; McCoy, M.R.; Hamed, I.A.; Ashour, M.B.; Hammock, B.D. Pesticide Residues in Vegetables and Fruits from Farmer Markets and Associated Dietary Risks. *Molecules* **2022**, *27*, 72. [CrossRef] [PubMed]
12. Jyoti, J.L.; Shelton, A.M.; Taylor, A.G. Film-coating seeds with chlorpyrifos for germination and control of cabbage maggot (Diptera:Anthomyiidae) on cabbage transplants. *J. Entomol. Sci.* **2003**, *38*, 553–565. [CrossRef]
13. Bundy, C.S.; Lewis, B. Impact of chlorpyrifos for pink bollworm control on secondary pests and beneficials. *Southwest. Entomol.* **2005**, *30*, 105–111.
14. Goh, W.L.; Yiu, P.H.; Wong, S.C.; Rajan, A. Safe use of chlorpyrifos for insect pest management in leaf mustard (*Brassica juncea* L. Coss.). *J. Food Agric. Env.* **2011**, *9*, 1064–1066.
15. Su, H.H.; Jiang, L.L.; Wang, H.T.; Yang, T.Z.; Harvey-Samuel, T.; Zhou, Q.X.; Lü, Y.B.; Yang, Y.Z. Sublethal effects of Bt toxin and chlorpyrifos on various Spodoptera exigua populations. *Entomol. Exp. Appl.* **2015**, *157*, 214–219. [CrossRef]
16. Hites, R.A. The Rise and Fall of Chlorpyrifos in the United States. *Environ. Sci. Technol.* **2021**, *55*, 1354–1358. [CrossRef]
17. John, E.M.; Shaike, J.M. Chlorpyrifos: Pollution and remediation. *Environ. Chem. Lett.* **2015**, *13*, 269–291. [CrossRef]
18. Wang, L.; Liu, Z.; Zhang, J.J.; Wu, Y.H.; Sun, H.W. Chlorpyrifos exposure in farmers and urban adults: Metabolic characteristic, exposure estimation, and potential effect of oxidative damage. *Environ. Res.* **2016**, *149*, 164–170. [CrossRef]
19. Rahman, H.U.U.; Asghar, W.; Nazir, W.; Sandhu, M.A.; Ahmed, A.; Khalid, N. A comprehensive review on chlorpyrifos toxicity with special reference to endocrine disruption: Evidence of mechanisms, exposures and mitigation strategies. *Sci. Total Environ.* **2021**, *755*, 142649. [CrossRef]
20. Tudi, M.; Yang, L.S.; Wang, L.; Lv, J.; Gu, L.J.; Li, H.R.; Peng, W.; Yu, Q.M.; Ruan, H.D.; Li, Q.; et al. Environmental and Human Health Hazards from Chlorpyrifos, Pymetrozine and Avermectin Application in China under a Climate Change Scenario: A Comprehensive Review. *Agriculture* **2023**, *13*, 1683. [CrossRef]
21. Guo, J.Q.; Zhang, J.M.; Wu, C.H.; Lv, S.L.; Lu, D.S.; Qi, X.J.; Jiang, S.; Feng, C.; Yu, H.X.; Liang, W.J.; et al. Associations of prenatal and childhood chlorpyrifos exposure with Neurodevelopment of 3-year-old children. *Environ. Pollut.* **2019**, *251*, 538–546. [CrossRef]
22. Rauh, V.A.; Garfinkel, R.; Perera, F.P.; Andrews, H.F.; Hoepner, L.; Barr, D.B.; Whitehead, R.; Tang, D.; Whyatt, R.W. Impact of prenatal chlorpyrifos exposure on neurodevelopment in the first 3 years of life among inner-city children. *Pediatrics* **2006**, *118*, E1845–E1859. [CrossRef]
23. Lee, J.E.; Kim, M.K.; Lee, J.Y.; Lee, Y.M.; Zoh, K.D. Degradation kinetics and pathway of 1H-benzotriazole during UV/chlorination process. *Chem. Eng. J.* **2019**, *359*, 1502–1508. [CrossRef]
24. Mansor, N.A.; Tay, K.S. Degradation of 5,5-diphenylhydantoin by chlorination and UV/chlorination: Kinetics, transformation by-products, and toxicity assessment. *Environ. Sci. Pollut. R* **2017**, *24*, 22361–22370. [CrossRef] [PubMed]
25. Qin, L.; Lin, Y.L.; Xu, B.; Hu, C.Y.; Tian, F.X.; Zhang, T.Y.; Zhu, W.Q.; Huang, H.; Gao, N.Y. Kinetic models and pathways of ronidazole degradation by chlorination, UV irradiation and UV/chlorine processes. *Water Res.* **2014**, *65*, 271–281. [CrossRef] [PubMed]
26. Yang, S.M.; Feng, Y.; Gao, D.; Wang, X.W.; Suo, N.; Yu, Y.Z.; Zhang, S.B. Electrocatalysis degradation of tetracycline in a three-dimensional aeration electrocatalysis reactor (3D-AER) with a flotation-tailings particle electrode (FPE): Physicochemical properties, influencing factors and the degradation mechanism. *J. Hazard. Mater.* **2021**, *407*, 18. [CrossRef]
27. Wang, Y.L.; Cai, N.C.; Huo, Y.D.; Chen, H. Electrochemical oxidation for the degradation of aniline on the SnO_2/Ti anode. *Acta Phys. Chim. Sin.* **2001**, *17*, 609–613. [CrossRef]
28. Zhou, M.H.; Wu, Z.C.; Wang, D.H. A novel electrocatalysis method for organic pollutants degradation. *Chin. Chem. Lett.* **2001**, *12*, 929–932.
29. Zhang, M.H.; Liu, G.H.; Song, K.; Wang, Z.Y.; Zhao, Q.L.; Li, S.J.; Ye, Z.F. Biological treatment of 2,4,6-trinitrotoluene (TNT) red water by immobilized anaerobic-aerobic microbial filters. *Chem. Eng. J.* **2015**, *259*, 876–884. [CrossRef]

30. Ji, Q.H.; Tabassum, S.; Yu, G.X.; Chu, C.F.; Zhang, Z.J. Determination of biological removal of recalcitrant organic contaminants in coal gasification waste water. *Environ. Technol.* **2015**, *36*, 2815–2824. [CrossRef]
31. Jiang, Y.; Wang, H.Y.; Shang, Y.; Yang, K. Simultaneous removal of aniline, nitrogen and phosphorus in aniline-containing wastewater treatment by using sequencing batch reactor. *Bioresour. Technol.* **2016**, *207*, 422–429. [CrossRef]
32. Goudarzi, M.; Abdulhusain, Z.H.; Salavati-Niasari, M. Low-cost and eco-friendly synthesis of Mn-doped T_2WO_4 nanostructures for efficient visible light photocatalytic degradation of antibiotics in water. *Sol. Energy* **2023**, *262*, 111912. [CrossRef]
33. Mehdizadeh, P.; Jamdar, M.; Mahdi, M.A.; Abdulsahib, W.K.; Jasim, L.S.; Yousefi, S.R.; Salavati-Niasari, M. Rapid microwave fabrication of new nanocomposites based on Tb-Co-O nanostructures and their application as photocatalysts under UV/Visible light for removal of organic pollutants in water. *Arab. J. Chem.* **2023**, *16*, 104579. [CrossRef]
34. Hafeez, A.; Shezad, N.; Javed, F.; Fazal, T.; Rehman, M.S.U.; Rehman, F. Synergetic effect of packed-bed corona-DBD plasma micro-reactor and photocatalysis for organic pollutant degradation. *Sep. Purif. Technol.* **2021**, *269*, 118728. [CrossRef]
35. Mmelesi, O.K.; Masunga, N.; Kuvarega, A.; Nkambule, T.T.; Mamba, B.B.; Kefeni, K.K. Cobalt ferrite nanoparticles and nanocomposites: Photocatalytic, antimicrobial activity and toxicity in water treatment. *Mat. Sci. Semicon. Proc.* **2021**, *123*, 105523. [CrossRef]
36. Masunga, N.; Mamba, B.B.; Kefeni, K.K. Trace samarium doped graphitic carbon nitride photocatalytic activity toward metanil yellow dye degradation under visible light irradiation. *Colloid. Surface A* **2020**, *602*, 125107. [CrossRef]
37. Rostami, M.; Jourshabani, M.; Davar, F.; Ziarani, G.M.; Badiei, A. Black TiO_2-g-C_3N_4 heterojunction coupled with MOF (ZIF-67)-derived Co_3S_4/nitrogen-doped carbon hollow nanobox. *J. Am. Ceram. Soc.* **2023**, *107*, 719–735. [CrossRef]
38. Ye, K.H.; Li, Y.; Yang, H.; Li, M.Y.; Huang, Y.C.; Zhang, S.Q.; Ji, H.B. An ultrathin carbon layer activated CeO_2 heterojunction nanorods for photocatalytic degradation of organic pollutants. *Appl. Catal. B Environ.* **2019**, *259*, 118085. [CrossRef]
39. Yang, X.F.; Qin, J.L.; Jiang, Y.; Chen, K.M.; Yan, X.H.; Zhang, D.; Li, R.; Tang, H. Fabrication of P25/Ag_3PO_4/graphene oxide heterostructures for enhanced solar photocatalytic degradation of organic pollutants and bacteria. *Appl. Catal. B-Environ.* **2015**, *166*, 231–240. [CrossRef]
40. Koe, W.S.; Lee, J.W.; Chong, W.C.; Pang, Y.L.; Sim, L.C. An overview of photocatalytic degradation: Photocatalysts, mechanisms, and development of photocatalytic membrane. *Environ. Sci. Pollut. R* **2020**, *27*, 2522–2565. [CrossRef] [PubMed]
41. Wen, X.J.; Shen, C.H.; Fei, Z.H.; Fang, D.; Liu, Z.T.; Dai, J.T.; Niu, C.G. Recent developments on AgI based heterojunction photocatalytic systems in photocatalytic application. *Chem. Eng. J.* **2020**, *383*, 21. [CrossRef]
42. Luan, J.F.; Niu, B.W.; Ma, B.B.; Yang, G.M.; Liu, W.L. Preparation and Property Characterization of In_2YSbO_7/$BiSnSbO_6$ Heterojunction Photocatalyst toward Photocatalytic Degradation of Indigo Carmine within Dye Wastewater under Visible-Light Irradiation. *Materials* **2022**, *15*, 6648. [CrossRef] [PubMed]
43. Soleimani, M.; Ghasemi, J.B.; Ziarani, G.M.; Karimi-Maleh, H.; Badiei, A. Photocatalytic degradation of organic pollutants, viral and bacterial pathogens using titania nanoparticles. *Inorg. Chem. Commun.* **2021**, *130*, 108688. [CrossRef]
44. Zhang, Q.H.; Gao, L.; Guo, J.K. Photocatalytic activity of nanosized TiO_2. *J. Inorg. Mater.* **2000**, *15*, 556–560.
45. Wold, A. Photocatalytic Properties of TIO_2. *Chem. Mater.* **1993**, *5*, 280–283. [CrossRef]
46. Yeber, M.C.; Rodríguez, J.; Freer, J.; Durán, N.; Mansilla, H.D. Photocatalytic degradation of cellulose bleaching effluent by supported TiO_2 and ZnO. *Chemosphere* **2000**, *41*, 1193–1197. [CrossRef] [PubMed]
47. Villasenor, J.; Reyes, P.; Pecchi, G. Photodegradation of pentachlorophenol on ZnO. *J. Chem. Technol. Biotechnol.* **1998**, *72*, 105–110. [CrossRef]
48. Dong, W.X.; Bao, Q.F.; Gu, X.Y.; Peng, G.; Zhao, X.G. C_3N_4/$CaTi_2O_5$ Composite: Synthesis and Photocatalytic Properties. *Chinese. J.Org. Chem.* **2017**, *33*, 292–298. [CrossRef]
49. Li, J.H.; Han, M.S.; Guo, Y.; Wang, F.; Sun, C. Fabrication of $FeVO_4$/Fe_2TiO_5 composite catalyst and photocatalytic removal of norfloxacin. *Chem. Eng. J.* **2016**, *298*, 300–308. [CrossRef]
50. Issarapanacheewin, S.; Wetchakun, K.; Phanichphant, S.; Kangwansupamonkon, W.; Wetchakun, N. A novel CeO_2/Bi_2WO_6 composite with highly enhanced photocatalytic activity. *Mater. Lett.* **2015**, *156*, 28–31. [CrossRef]
51. Hunge, Y.M.; Yadav, A.A.; Kang, S.W. Photocatalytic Degradation of Eriochrome Black-T Using $BaWO_4$/MoS_2 Composite. *Catalysts* **2022**, *12*, 11. [CrossRef]
52. Zou, Z.G.; Ye, J.H.; Abe, R.; Arakawa, H. Photocatalytic decomposition of water with Bi_2InNbO_7. *Catal. Lett.* **2000**, *68*, 235–239. [CrossRef]
53. Cui, Y.B.; Luan, J.F. Synthesis, crystal structure, photodegradation kinetics and photocatalytic activity of novel photocatalyst $ZnBiYO_4$. *J. Environ. Sci.* **2015**, *29*, 51–61. [CrossRef]
54. Ajmal, A.; Majeed, I.; Malik, R.N.; Idriss, H.; Nadeem, M.A. Principles and mechanisms of photocatalytic dye degradation on TiO_2 based photocatalysts: A comparative overview. *RSC. Adv.* **2014**, *4*, 37003–37026. [CrossRef]
55. Tu, W.G.; Zhou, Y.; Zou, Z.G. Versatile Graphene-Promoting Photocatalytic Performance of Semiconductors: Basic Principles, Synthesis, Solar Energy Conversion, and Environmental Applications. *Adv. Funct. Mater.* **2013**, *23*, 4996–5008. [CrossRef]
56. Wang, S.B.; Wang, F.F.; Su, Z.M.; Wang, X.N.; Han, Y.C.; Zhang, L.; Xiang, J.; Du, W.; Tang, N. Controllable Fabrication of Heterogeneous p-TiO_2 QDs@g-C_3N_4 p-n Junction for Efficient Photocatalysis. *Catalysts* **2019**, *9*, 439. [CrossRef]
57. Wang, W.Z.; Huang, X.W.; Wu, S.; Zhou, Y.X.; Wang, L.J.; Shi, H.L.; Liang, Y.J.; Zou, B. Preparation of p-n junction Cu_2O/$BiVO_4$ heterogeneous nanostructures with enhanced visible-light photocatalytic activity. *Appl. Catal. B-Environ.* **2013**, *134*, 293–301. [CrossRef]

58. Xu, H.; Xu, Y.G.; Li, H.M.; Xia, J.X.; Xiong, J.; Yin, S.; Huang, C.J.; Wan, H.L. Synthesis, characterization and photocatalytic property of AgBr/$BiPO_4$ heterojunction photocatalyst. *Dalton Trans.* **2012**, *41*, 3387–3394. [CrossRef]
59. Cheng, T.T.; Gao, H.J.; Sun, X.F.; Xian, T.; Wang, S.F.; Yi, Z.; Liu, G.R.; Wang, X.X.; Yang, H. An excellent Z-scheme Ag_2MoO_4/$Bi_4Ti_3O_{12}$heterojunction photocatalyst: Construction strategy and application in environmental purification. *Adv. Powder Technol.* **2021**, *32*, 951–962. [CrossRef]
60. Fattah, W.I.A.; Gobara, M.M.; El-Hotaby, W.; Mostafa, S.F.M.; Ali, G.W. Coating stainless steel plates with Ag/TiO_2 for chlorpyrifos decontamination. *Mater. Res. Express.* **2016**, *3*, 055009. [CrossRef]
61. Pathania, D.; Sharma, A.; Kumar, S.; Srivastava, A.K.; Kumar, A.; Singh, L. Bio-synthesized Cu-ZnO hetro-nanostructure for catalytic degradation of organophosphate chlorpyrifos under solar illumination. *Chemosphere* **2021**, *277*, 130315. [CrossRef]
62. Luan, J.F.; Wei, Z.J.; Niu, B.W.; Yang, G.M.; Huang, C.S.; Ma, B.B.; Liu, W.L. Synthesis, Property Characterization and Photocatalytic Activity of the Ag_3PO_4/Gd_2BiTaO_7 Heterojunction Catalyst under Visible Light Irradiation. *Catalysts* **2022**, *12*, 22. [CrossRef]
63. Wang, J.H.; Zou, Z.G.; Ye, J.H. Synthesis, structure and photocatalytic property of a new hydrogen evolving photocatalyst Bi2InTaO7. In *Functionally Graded Materials Vii*; Pan, W., Gong, J., Zhang, L., Chen, L., Eds.; Trans Tech Publications Ltd.: Zurich-Uetikon, Switzerland, 2003; Volume 423–424, pp. 485–490.
64. Kohno, M.; Ogura, S.; Sato, K.; Inoue, Y. Properties of photocatalysts with tunnel structures: Formation of a surface lattice O-radical by the UV irradiation of $BaTi_4O_9$ with a pentagonal-prism tunnel structure. *Chem. Phys. Lett.* **1997**, *267*, 72–76. [CrossRef]
65. Kudo, A.; Kato, H.; Nakagawa, S. Water splitting into H_2 and O_2 on new $Sr_2M_2O_7$ (M = Nb and Ta) photocatalysts with layered perovskite structures:: Factors affecting the photocatalytic activity. *J. Phys. Chem. B* **2000**, *104*, 571–575. [CrossRef]
66. Wiegel, M.; Middel, W.; Blasse, G. Influence of ns(2) ions on the luminescence of niobates and tantalates. *J. Mater. Chem.* **1995**, *5*, 981–983. [CrossRef]
67. Luan, J.F.; Ma, B.B.; Yao, Y.; Liu, W.L.; Niu, B.W.; Yang, G.M.; Wei, Z.J. Synthesis, Performance Measurement of Bi_2SmSbO_7/$ZnBiYO_4$ Heterojunction Photocatalyst and Photocatalytic Degradation of Direct Orange within Dye Wastewater under Visible Light Irradiation. *Materials* **2022**, *15*, 3986. [CrossRef] [PubMed]
68. Monshi, A.; Foroughi, M.R.; Monshi, M.R. Modified Scherrer Equation to Estimate More Accurately Nano-Crystallite Size Using XRD. *World J. Nano Sci. Eng.* **2012**, *2*, 154–160. [CrossRef]
69. Nasiri, S.; Rabiei, M.; Palevicius, A.; Janusas, G.; Vilkauskas, A.; Nutalapati, V.; Monshi, A. Modified Scherrer equation to calculate crystal size by XRD with high accuracy, examples Fe_2O_3, TiO_2 and V_2O_5. *Nano Trends* **2023**, *3*, 100015. [CrossRef]
70. Burton, A.W.; Ong, K.; Rea, T.; Chan, I.Y. On the estimation of average crystallite size of zeolites from the Scherrer equation: A critical evaluation of its application to zeolites with one-dimensional pore systems. *Microporous Mesoporous Mater.* **2009**, *117*, 75–90. [CrossRef]
71. Shaishta, N.; Khan, W.U.; Mane, S.K.B.; Hayat, A.; Zhou, D.D.; Khan, J.; Mehmood, N.; Inamdar, H.K.; Manjunatha, G. Red-emitting $CaSc_2O_4$:Eu^{3+} phosphor for NUV-based warm white LEDs: Structural elucidation and Hirshfeld surface analysis. *Int. J. Energy Res.* **2020**, *44*, 8328–8339. [CrossRef]
72. Goh, K.H.; Haseeb, A.; Wong, Y.H. Effect of Oxidation Temperature on Physical and Electrical Properties of Sm_2O_3 Thin-Film Gate Oxide on Si Substrate. *J. Electron. Mater.* **2016**, *45*, 5302–5312. [CrossRef]
73. Kaviyarasu, K.; Sajan, D.; Devarajan, P.A. A rapid and versatile method for solvothermal synthesis of Sb_2O_3 nanocrystals under mild conditions. *Appl. Nanosci.* **2013**, *3*, 529–533. [CrossRef]
74. Rada, S.; Rus, L.; Rada, M.; Zagrai, M.; Culea, E.; Rusu, T. Compositional dependence of structure, optical and electrochemical properties of antimony(III) oxide doped lead glasses and vitroceramics. *Ceram. Int.* **2014**, *40*, 15711–15716. [CrossRef]
75. Achehboune, M.; Khenfouch, M.; Boukhoubza, I.; Leontie, L.; Doroftei, C.; Carlescu, A.; Bulai, G.; Mothudi, B.; Zorkani, I.; Jorio, A. Microstructural, FTIR and Raman spectroscopic study of Rare earth doped ZnO nanostructures. In Proceedings of the Nanosmat Mediterrane Conference, Fac Sci Rabat, Rabat, Morocco, 2 May–4 June 2009; pp. 319–323.
76. Bosca, M.; Pop, L.; Borodi, G.; Pascuta, P.; Culea, E. XRD and FTIR structural investigations of erbium-doped bismuth-lead-silver glasses and glass ceramics. *J. Alloys Compd.* **2009**, *479*, 579–582. [CrossRef]
77. Isari, A.A.; Hayati, F.; Kakavandi, B.; Rostami, M.; Motevassel, M.; Dehghanifard, E. N, Cu co-doped TiO_2@functionalized SWCNT photocatalyst coupled with ultrasound and visible-light: An effective sono-photocatalysis process for pharmaceutical wastewaters treatment. *Chem. Eng. J.* **2020**, *392*, 16. [CrossRef]
78. Karimi, B.; Habibi, M.H. High photocatalytic activity of light-driven Fe_2TiO_5 nanoheterostructure toward degradation of antibiotic metronidazole. *J. Ind. Eng. Chem.* **2019**, *80*, 292–300. [CrossRef]
79. Berg, R.W.; Thorup, N. The reaction between ZnO and molten $Na_2S_2O_7$ or $K_2S_2O_7$ forming $Na_2Zn(SO_4)_2$ or $K_2Zn(SO_4)_2$, studied by Raman spectroscopy and X-ray diffraction. *Inorg. Chem.* **2005**, *44*, 3485–3493. [CrossRef] [PubMed]
80. Tsaryuk, V.I.; Zhuravlev, K.P.; Szostak, R.; Vologzhanina, A.V. Structure, Luminescence, and Raman Spectroscopy of Europium and Terbium Dipivaloylmethanates and Other β-Diketonates with 2,2′-Bipyridine. *J. Struct. Chem.* **2020**, *61*, 1026–1037. [CrossRef]
81. Chahine, A.; Et-tabirou, M.; Pascal, J.L. FTIR and Raman spectra of the Na_2O-CuO-Bi_2O_3-P_2O_5 glasses. *Mater. Lett.* **2004**, *58*, 2776–2780. [CrossRef]
82. Hadjiev, V.G.; Iliev, M.N.; Sasmal, K.; Sun, Y.Y.; Chu, C.W. Raman spectroscopy of R FeAsO (R = Sm, La). *Phys. Rev. B* **2008**, *77*, 3. [CrossRef]

83. Refat, M.S.; Elsabawy, K.M. Infrared spectra, Raman laser, XRD, DSC/TGA and SEM investigations on the preparations of selenium metal, (Sb_2O_3, Ga_2O_3, SnO and HgO) oxides and lead carbonate with pure grade using acetamide precursors. *Bull. Mater. Sci.* **2011**, *34*, 873–881. [CrossRef]
84. Gilliam, S.J.; Jensen, J.O.; Banerjee, A.; Zeroka, D.; Kirkby, S.J.; Merrow, C.N. A theoretical and experimental study of Sb_4O_6: Vibrational analysis, infrared, and Raman spectra. *Spectrochim. Acta Part A Mol. Biomol. Spectrosc.* **2004**, *60*, 425–434. [CrossRef] [PubMed]
85. Luan, J.; Hao, L.; Yao, Y.; Wang, Y.; Yang, G.; Li, J. Preparation and Property Characterization of Sm_2EuSbO_7/$ZnBiSbO_5$ Heterojunction Photocatalyst for Photodegradation of Parathion Methyl under Visible Light Irradiation. *Molecules* **2023**, *28*, 7722. [CrossRef] [PubMed]
86. Uwamino, Y.; Ishizuka, T.; Yamatera, H. X-ray photoelectron-spectroscopy of rare-earth compounds. *J. Electron Spectrosc. Relat. Phenom.* **1984**, *34*, 67–78. [CrossRef]
87. Izquierdo, R.; Sacher, E.; Yelon, A. X-ray photoelectron-spectra of antimony oxides. *Appl. Surf. Sci.* **1989**, *40*, 175–177. [CrossRef]
88. Birchall, T.; Connor, J.A.; Hillier, I.H. High-energy photoelectron-spectroscopy of some antimony compounds. *J. Chem. Soc. Dalton Trans.* **1975**, 2003–2006. [CrossRef]
89. Benvenutti, E.V.; Gushikem, Y.; Vasquez, A.; Decastro, S.C.; Zaldivar, G.A.P. X-ray photoelectron-spectroscopy and mossbauer-spectroscopy study of iron(iii) and antimony(v) oxides grafted onto a silica-gel surface. *J. Chem. Soc. Chem. Commun.* **1991**, 1325–1327. [CrossRef]
90. Dake, L.S.; Baer, D.R.; Zachara, J.M. Auger parameter measurements of zinc-compounds relevant to zinc transport in the environment. *Surf. Interface Anal.* **1989**, *14*, 71–75. [CrossRef]
91. Morgan, W.E.; Stec, W.J.; Van Wazer, J.R. Inner-orbital binding-energy shifts of antimony and bismuth compounds. *Inorg. Chem.* **1973**, *12*, 953–955. [CrossRef]
92. Ettema, A.; Haas, C. AN X-ray photoemission spectroscopy study of interlayer charge-transfer in some misfit layer compounds. *J. Phys.-Condens. Matter* **1993**, *5*, 3817–3826. [CrossRef]
93. Wagner, C.D.; Zatko, D.A.; Raymond, R.H. Use of the oxygen kll auger lines in identification of surface chemical-states by electron-spectroscopy for chemical-analysis. *Anal. Chem.* **1980**, *52*, 1445–1451. [CrossRef]
94. Nowak, M.; Kauch, B.; Szperlich, P. Determination of energy band gap of nanocrystalline SbSI using diffuse reflectance spectroscopy. *Rev. Sci. Instrum.* **2009**, *80*, 3. [CrossRef]
95. Zhou, F.; Kang, K.S.; Maxisch, T.; Ceder, G.; Morgan, D. The electronic structure and band gap of $LiFePO_4$ and $LiMnPO_4$. *Solid State Commun.* **2004**, *132*, 181–186. [CrossRef]
96. Butler, M.A.; Ginley, D.S.; Eibschutz, M. Photoelectrolysis with $YFeO_3$ electrodes. *J. Appl. Phys.* **1977**, *48*, 3070–3072. [CrossRef]
97. Tauc, J.; Grigorovici, R.; Vancu, A.J.p.s.s. Optical properties and electronic structure of amorphous germanium. *Phys. Status Solidi.* **1966**, *15*, 627–637. [CrossRef]
98. Makula, P.; Pacia, M.; Macyk, W. How To Correctly Determine the Band Gap Energy of Modified Semiconductor Photocatalysts Based on UV-Vis Spectra. *J. Phys. Chem. Lett.* **2018**, *9*, 6814–6817. [CrossRef] [PubMed]
99. Cheng, X.W.; Yu, X.J.; Xing, Z.P.; Yang, L.S. Synthesis and characterization of N-doped TiO_2 and its enhanced visible-light photocatalytic activity. *Arab. J. Chem.* **2016**, *9*, S1706–S1711. [CrossRef]
100. Ananpattarachai, J.; Kajitvichyanukul, P.; Seraphin, S. Visible light absorption ability and photocatalytic oxidation activity of various interstitial N-doped TiO_2 prepared from different nitrogen dopants. *J. Hazard. Mater.* **2009**, *168*, 253–261. [CrossRef] [PubMed]
101. Kanmoni, V.G.G.; Daniel, S.; Raj, G.A.G. Photocatalytic degradation of chlorpyrifos in aqueous suspensions using nanocrystals of ZnO and TiO_2. *React. Kinet. Mech. Catal.* **2012**, *106*, 325–339. [CrossRef]
102. Poonam, V.; Poonam, D.D. Photocatalytic degradability of insecticide Chlorpyrifos over UV irradiated Titanium dioxide in aqueous phase. *Int. J. Environ. Sci.* **2012**, *3*, 743–755.
103. Baharvand, A.; Ali, R.; Yusof, A.M.; Ibrahim, A.N.; Chandren, S.; Nur, H. Preparation of Anatase Hollow TiO_2 Spheres and Their Photocatalytic Activity in the Photodegradation of Chlorpyrifos. *J. Chin. Chem. Soc.* **2014**, *61*, 1211–1216. [CrossRef]
104. Majhi, D.; Bhoi, Y.P.; Samal, P.K.; Mishra, B.G. Morphology controlled synthesis and photocatalytic study of novel CuS-$Bi_2O_2CO_3$ heterojunction system for chlorpyrifos degradation under visible light illumination. *Appl. Surf. Sci.* **2018**, *455*, 891–902. [CrossRef]
105. Nekooie, R.; Shamspur, T.; Mostafavi, A. Novel CuO/TiO_2/PANI nanocomposite: Preparation and photocatalytic investigation for chlorpyrifos degradation in water under visible light irradiation. *J. Photochem. Photobiol. A Chem.* **2021**, *407*, 113038. [CrossRef]
106. Esfandian, H.; Cherati, M.R.; Khatirian, M. Electrochemical behavior and photocatalytic performance of chlorpyrifos pesticide decontamination using Ni-doped ZnO-TiO2 nanocomposite. *Inorg. Chem. Commun.* **2024**, *159*, 111750. [CrossRef]
107. Balakrishnan, G.; Velavan, R.; Batoo, K.M.; Raslan, E.H. Microstructure, optical and photocatalytic properties of MgO nanoparticles. *Results. Phys.* **2020**, *16*, 4. [CrossRef]
108. Ali, T.; Tripathi, P.; Azam, A.; Raza, W.; Ahmed, A.S.; Ahmed, A.; Muneer, M. Photocatalytic performance of Fe-doped TiO_2 nanoparticles under visible-light irradiation. *Mater. Res. Express.* **2017**, *4*, 12. [CrossRef]
109. Chen, J.; Zhao, X.; Kim, S.G.; Park, N.G. Multifunctional Chemical Linker Imidazoleacetic Acid Hydrochloride for 21% Efficient and Stable Planar Perovskite Solar Cells. *Adv. Mater.* **2019**, *31*, 1902902. [CrossRef]
110. Chen, J.; Kim, S.G.; Ren, X.; Jung, H.S.; Park, N.G. Effect of bidentate and tridentate additives on the photovoltaic performance and stability of perovskite solar cells. *J. Mater. Chem. A* **2019**, *7*, 4977–4987. [CrossRef]

111. Jiang, L.B.; Yuan, X.Z.; Zeng, G.M.; Liang, J.; Chen, X.H.; Yu, H.B.; Wang, H.; Wu, Z.B.; Zhang, J.; Xiong, T. In-situ synthesis of direct solid-state dual Z-scheme WO_3/g-C_3N_4/Bi_2O_3 photocatalyst for the degradation of refractory pollutant. *Appl. Catal. B-Environ.* **2018**, *227*, 376–385. [CrossRef]
112. Franco-Perez, M.; Gazquez, J.L. Electronegativities of Pauling and Mulliken in Density Functional Theory. *J. Phys. Chem. A* **2019**, *123*, 10065–10071. [CrossRef]
113. Mousavi, M.; Habibi-Yangjeh, A.; Abitorabi, M. Fabrication of novel magnetically separable nanocomposites using graphitic carbon nitride, silver phosphate and silver chloride and their applications in photocatalytic removal of different pollutants using visible-light irradiation. *J. Colloid Interface Sci.* **2016**, *480*, 218–231. [CrossRef] [PubMed]
114. Cao, W.; Jiang, C.Y.; Chen, C.; Zhou, H.F.; Wang, Y.P. A novel Z-scheme CdS/$Bi_4O_5Br_2$ heterostructure with mechanism analysis: Enhanced photocatalytic performance. *J. Alloys Compd.* **2021**, *861*, 12. [CrossRef]
115. Xu, S.; Gong, S.Q.; Jiang, H.; Shi, P.H.; Fan, J.C.; Xu, Q.J.; Min, Y.L. Z-scheme heterojunction through interface engineering for broad spectrum photocatalytic water splitting. *Appl. Catal. B-Environ.* **2020**, *267*, 12. [CrossRef]